NASA Technical Memorandum 80207

HEATING-RATE MEASUREMENTS OVER 30°

AND 40° (HALF-ANGLE) BLUNT CONES IN

AIR AND HELIUM IN THE LANGLEY

EXPANSION TUBE FACILITY

N. M. Reddy

March 1980
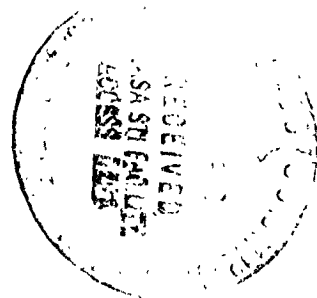
HEATING-RATE MEASUREMENTS OVER 30° AND 40° (HALF-ANGLE) BLUNT CONES IN AIR AND HELIUM IN THE LANGLEY EXPANSION TUBE FACILITY

N. M. Reddy*
Langley Research Center

SUMMARY

Convective heat-transfer measurements were made on the conical portion of spherically blunted cones (30° and 40° half angle) in the Langley expansion tube. The test gases used were helium and air; flow velocities were about 6.8 km/sec for helium and about 5.1 km/sec for air. The measured heating rates were compared with calculated results using a viscous shock-layer computer code. For air, various techniques to determine flow velocity yielded nearly identical results, but for helium the flow velocity varied by as much as 8 percent depending on which technique was used. The measured heating rates were in satisfactory agreement with calculation for helium test gas if the higher flow velocity was used, but for air and for helium assuming the lower flow velocity,the measurements were significantly greater than theory and the discrepancy increased with increasing distance along the cone.

INTRODUCTION

Determination of windward side heating rates during entry of the Space Shuttle Orbiter is very difficult. Analytical methods for calculating flow fields over complex configurations are as yet in a developmental stage, are costly, cumbersome, and limited in scope of variables. The extent of experimental data for such configurations is also limited, particularly for high velocity flow conditions. One approximation which has been made to permit calculation of the windward heating distribution on a vehicle at high angle of attack is to assume the flow along the windward centerline is similar to that of a cone whose half-angle is equal to the vehicle's local slope relative to the velocity vector. Several methods are available to the engineer to calculate the flow and heat-transfer rate for[1] the equivalent blunted cone at zero angle of attack. The critical heating rates on windward surfaces of the space shuttle are expected to occur at altitudes between 61 and 76 kilometers (200,000 and 250,000 ft.). In an effort to simulate the shuttle flow field, total flow-field calculations for blunt spherical nose cones (half-angle 30° and 40°) have been presented in reference 1. This analysis consisted of defining the complete flow field around blunted cones for assumed equilibrium and reacting gas cases. The axial length of the blunt cones was assumed to be 30.5 meters (100 ft.). This analysis (ref. 1) was mainly concerned with delineating in detail the real-gas effects in the boundary layer and their effect on the surface skin friction and heat transfer.

---

*NRC-Senior Research Associate, on leave from Indian Institute of Science, Bangalore, India.

The simulation capabilities of various Langley facilities have been also assessed in reference 1. The facilities considered are the Mach 8 variable density wind tunnel, Mach 20 helium tunnel, Mach 20 nitrogen tunnel, and the Mach 6 Freon (CF_4) tunnel. However, no simulation capability of the expansion tube facility is assessed in reference 1. The results showed that the best simulation of the inviscid flow field (shock standoff distance, edge Mach number) was provided by the CF_4 facility. The laminar heating simulation provided by all facilities was equivalent. It was concluded in reference 1 that natural boundary-layer transition is unlikely except in the variable density wind tunnel, especially at higher stagnation pressure level. Based on the results presented, the authors of reference 1 have concluded that investigations of two types would be required to verify the analytical results, namely (a) basic investigations of boundary-layer profiles combined with skin friction and heat-transfer measurements on relatively simple cylindrical shapes, and (b) aerodynamic heating tests on blunt-cone configurations of the type analyzed in reference 1.

The present investigation measured the heating-rate distributions over blunt cones of 30° and 40° half-angle in the Langley expansion tube facility with helium as well as air as test gases. The purpose of the present study is to present hypersonic cone heating data at both perfect-gas and real-gas conditions. The measured heating rates have been compared with computed values (ref. 2). An attempt has been made to measure heating rates within an accuracy of 4 to 5 percent by using two different and independent methods to deduce heating rates. Based on the results of the present investigation, some conclusions are drawn regarding the accuracy of heating-rate measurements and their comparison with the computed values.

SYMBOLS

a_1	speed of sound in driven tube
c_p	coefficient of specific heat at constant pressure for quartz substrate
C	capacitance in the analog network
D	amplification factor for analog circuit
E	voltage across the thin film and also across the analog circuit
ΔE	voltage change across the thin film
E_o	initial voltage across the thin film
E_b	battery voltage
I	current through the gage

2

I_o	initial current through the gage
i	current through the analog network
k	coefficient of thermal conductivity of quartz substrate
$M_{s,1}$	incident shock wave in the intermediate section
$M_{s,10}$	incident shock wave in the acceleration section
M_∞	free-stream Mach number
M_2	flow Mach number behind the incident shock wave $M_{s,1}$
p_∞	free-stream pressure
p_2	pressure behind shock wave
p_1	initial pressure in the intermediate section or driven tube in the calibration shock tube
Pr	Prandtl number
p_{10}	initial pressure in the acceleration section
q	heat-transfer rate (watts/m^2)
q_{st}	stagnation-point heat-transfer rate
r	expansion tube radius
R_n	body nose radius
R	resistance in the analog network (also gage resistance in appendix C)
$\left.\begin{array}{l} R_1, R_2, \\ R_3, R_4 \end{array}\right\}$	defined in appendix C
R_0	initial resistance of gage
Re_∞	free-stream Reynolds number/meter
s	distance along the body
t	time
T_∞	free-stream temperature
T	temperature of quartz substrate

3

U_e velocity at the boundary-layer edge at the stagnation point

U_2 flow velocity behind shock wave $M_{s,1}$

U_5 flow velocity in region ⑤ (fig. 1)

$U_{s,10}$ shock velocity in the acceleration section

$U_{s,1}$ shock velocity in the intermediate section

U_{27-31} shock velocity determined between station numbers 27 and 31

$U_{average}$ shock velocity at model location from average curve fit

V_a voltage across the first resistance in the analog network

x distance from tube centerline normal to flow axis

z_e distance from tube exit

α thin-film temperature coefficient of resistance

β defined as $\beta = (k\rho C_p)^{1/2}$

ρ density of quartz substrate

ε_{10} density ratio across the shock $M_{s,10}$

ρ_e density at the boundary-layer edge at the stagnation point

μ_e viscosity at boundary-layer edge

θ cone semivertex angle

λ dummy variable (eq. (1))

FACILITY AND TEST CONDITIONS

Expansion Tube Facility

Several papers (refs. 3 to 9) have been published concerning the description and performance estimation of the expansion tube facility at the Langley Research Center. It consists of a driver section (2.44-m long and 0.165-m-dia.), an intermediate section (7.49-m long and 0.152-m dia.) and an acceleration section (14.12-m long and 0.152-m dia.). The driver section is pressurized at ambient temperature with a gas having a high speed of sound. For the present tests, hydrogen

was used as the driver gas. The intermediate section is evacuated and filled with the desired test gas with pressure p_1 at ambient temperature. The acceleration section was also evacuated along with the dump tank to a very low pressure and filled with the same gas as the selected test gas but to a much lower pressure level p_{10} at room temperature. The pressure difference between the intermediate and acceleration sections was maintained by a thin secondary diaphragm made of polyester film ranging in thickness from 3.175 to 25.4 μm. The main diaphragm between the driver and the intermediate sections was made of stainless steel. The test models were positioned 0.038 m downstream from the acceleration tube exit. Flow through the acceleration section exhausts into a dump tank; hence, models are tested in an open jet. A detailed description of the basic components and auxiliary equipment of the Langley expansion tube is presented in references 9 and 10.

The operating sequence for the expansion tube is shown schematically in figure 1. The operating sequence starts with rupture of the high-pressure primary diaphragm. This creates an incident shock wave which travels down the intermediate section until it encounters the secondary diaphragm. The low-pressure secondary diaphragm will be ruptured due to impact of incident shock wave. This creates a secondary incident shock wave which propagates into the low-pressure acceleration gas while an upstream expansion wave moves into the test gas. In passing through this upstream expansion wave, which is being washed downstream since the shock-heated gas is supersonic, the test gas undergoes an isentropic unsteady expansion resulting in an increase in the flow velocity and Mach number.

Free-Stream Flow Calibration

Flow uniformity.- Extensive flow calibration in the expansion tube facility for the case of helium test gas has been recently completed and reported in reference 9. Pitot pressure profiles at various distances downstream of acceleration tube exit in the case of helium test gas (p_1 = 3447 N/m^2; p_{10} = 16.0 N/m^2, t = 200 μsecs) are shown in figure 2 (taken from ref. 9). From this study it was found that for the initial conditions used in the present tests, the pitot survey shows uniform flow region of about 7 to 8 cm in diameter between 1 and 20 cm downstream of the acceleration tube exit. Calibrations for air test gas have shown a similar test core size.

Free-stream flow quantities.- The free-stream flow quantities were computed from the real-gas computer program of reference 11. At least three flow quantities (either predicted or measured) have to be known to obtain other flow quantities from the computer program of reference 11. Calculated flow quantities based on test section flow measurements are considered to be superior to those based on initial state variables because of deviations from theoretical prediction. The usual procedure would be to use the measured wall static pressure and shock velocity near the acceleration tube exit in each run and the measured pitot pressure in the test section in a repeated run as the three required flow

5

quantities to compute the other free-stream flow quantities from the computer program of reference 11. In the expansion tube facility the repeatability of runs as ascertained from the measured shock velocity is good in almost all cases with air and helium as test gases. But the inherent nonideal effects (viscous, real-gas and shock-reflection phenomena at the secondary diaphragm) might affect the flow quantities in the test section significantly in each run. In this sense, the repeatability as ascertained from the measured shock velocity may not be sufficient. Therefore, in the present investigation it was decided to measure simultaneously the pitot pressure in addition to wall static pressure and shock velocity in each run. In the present investigation the pitot pressure was measured by installing a small pressure transducer (2.5-mm dia.) in the blunt nose of each of the heat-transfer cone models. Since the transducer size was very small, the effects on flow over the model due to curvature change near the nose region were assumed to be negligible.

Free-stream static pressure.- The wall static pressure, which was measured at a station 0.026 m upstream of the acceleration tube exit, by using a commercial piezoelectric pressure transducer, was assumed equal to the free-stream static pressure (ref. 9). The transducer was connected to a charge amplifier, the output of which was displayed on an oscilloscope.

Pitot pressure.- The pitot pressure was measured by using a piezoresistive pressure transducer with a fully active semiconductor wheatstone bridge which has a nominal sensitivity of about 0.0725 mv/ kN/m^2 (0.5 mv/psi). These gages were calibrated before each run by using a step pressure input and the pitot pressure variation during each run was recorded and stored at 2.5-μsec intervals in a waveform recorder.

Free-stream velocity.- The free-stream velocity U_5 in region 5 (fig. 1) is ideally equal to the acceleration gas/test-gas interface velocity. This velocity is normally not measured but deduced from the measured shock velocity $U_{s,10}$. Ideal shock tube theory shows that the separation distance between the shock and interface increases linearly with distance from the diaphragm station. However, the shock tube wall boundary layer causes the incident shock to decelerate and the interface to accelerate and thus approach the same value. It is shown in reference 9 that for helium test gas, for values of p_{10} less than 50 N/m^2, the interface velocity U_5 is essentially equal to the incident shock velocity $U_{s,10}$. This assumption was made in the present investigation. In the case of air test gas also the same assumption ($U_5 \simeq U_{s,10}$) can be made since the p_{10} value used was 6.7 N/m^2. The dominant fact here is that the maximum separation distance between shock and interface has been approached for the p_{10} range understudy. From the preceding discussion it is obvious that an accurate measurement of shock velocity near the acceleration tube exit is essential for an accurate prediction of test section flow velocity.

6

The shock velocity $U_{s,10}$ in the acceleration section is measured routinely in the Langley expansion tube facility by time-of-arrival data gages mounted in the tube wall. More details are found in references 10 and 12. The time-of-arrival data were obtained by counter readings which were triggered by signals obtained from wall-mounted thin-film heat-transfer gages along the length of the acceleration section. Typical variations of shock velocity $U_{s,10}$ in helium and air test gases are shown in figures 3 and 4, respectively. A straight-line fit to the measured data is also shown in figures 3 and 4. The velocity at the tube exit given by the straight-line fit is given in table I for all the runs. Comparisons of figures 3 and 4 show that helium exhibited more scatter in the velocity measurements, because of the lower signal levels. Also, some counters in several runs gave completely erroneous readings, especially in helium, and these readings had to be omitted in fitting a straight line to the data.

Because of the importance of an accurate velocity determination at the test section, an examination was made of the method for determining velocity. The shock velocity between the last two stations (station numbers 27 and 31 which are 1.554 m apart) was deduced by using corresponding counter readings as well as the time interval measured from the oscilloscope film of heat-transfer gage outputs. These values are also shown in table I. The wall pressure gage film data between these two stations were also available and velocity deduced from these data is also shown in table I. The time sweep of all scopes was calibrated with a time mark generator and corrections for sweep rate were applied wherever necessary. It is apparent from table I that the shock velocities obtained by different methods for any given run do not agree with each other.

In the case of air test gas, the shock velocities deduced from the counter reading between stations 27 and 31 are believed to be suspect since the output from the heat-transfer gage at station 27 went negative immediately after the shock passage before it recovered back to its normal behavior and this might have affected the counter reading. The discrepancy noticed between velocities obtained from heat transfer and wall pressure film data in table I is somewhat surprising since the method used is the same. However, it was observed that the heat-transfer gage's response at stations 27 and 31 was much slower than the pressure gage's response at the same stations, which is perhaps due to thick coating on the heat-transfer gages. For this reason, the velocity obtained from the pressure film data between stations 27 and 31 may be of superior value. It is interesting to note that in the case of air, the differences between the velocities obtained from the straight-line fit to the data over the entire tube length and the pressure film data are very small.

In the case of helium the differences between velocities obtained from different methods are much more than those obtained in air. The output from the heat-transfer gage at station 27 in the case of helium

did not go negative, unlike the case of air, probably due to negligible ionization. But the response was too slow and the signal level was very small which might have affected the counters significantly.

Because of these discrepancies, the theoretical heating predictions were computed for both the velocity deduced from the curve fit ($U_{average}$) and that obtained from the pressure data (U_{27-31}) for the helium runs. For air runs, the difference was not significant so only U_{27-31} was used to compute heating rates. Flow-state calculations were based on U_{27-31}.

FABRICATION AND CALIBRATION OF THIN-FILM GAGES

Thin-film heat-transfer gages were fabricated by sputtering palladium on quartz substrates. The quartz substrates were fabricated with proper radius of curvature to fit the cone surface. The palladium film was sputtered over the entire top surface of the substrate and then the thin film in a serpentine pattern (fig. 5) was etched by using a photoetching process. The ends of the thin film are joined by a thick film in the sides and wires were soldered to the thick film. During development of this technique it was found that a thin coat of chromium (sputtering time 30 secs) on the substrate before palladium application improved the thin-film adherence to substrate enormously. The sputtering time for palladium film was 5 to 6 minutes. A coat of silicon dioxide (sputtering time 7 to 8 minutes) was sputtered on top of the palladium film to avoid possible shorting across the thin film due to ionization in the test gas. About 14 to 16 gages at nearly 3 mm apart were fabricated on each substrate (fig. 5). The quality control was such that all the films were identical in their geometrical characteristics; the resistance of each film was within a few percent of each other. The resistance value varied between 75 and 100 Ω for different batches.

Two types of calibrations are required for any thin film to be used as a quantitative heat-transfer measuring device, namely, the temperature coefficient of resistance α and the substrate property $\beta \equiv (k\rho c_p)^{1/2}$. The temperature coefficient of resistance α(ohm/ohm-k) was determined for each film at four different temperatures by heating the substrates in a controlled furnace and the α deduced by a computer program. Typical data for a substrate are given in table II. This method is believed to give α with an accuracy of 2 to 3 percent. The standard deviation in α between different gages is within 0.6 percent as shown in table II. This confirms the high degree of quality control maintained during gage fabrication.

The value of β for the quartz substrate cannot be obtained from the available bulk physical properties of quartz since uncertainties that exist in the physical properties evaluation are unacceptable in the present type of investigation. Furthermore, it is well established

8

that the physical behavior of quartz substrate immediately behind the
thin film will be different than the bulk substrate due to the presence
of thin film which is actually fired on to the substrate surface.
Therefore, several techniques (refs. 13-15) are available to determine
the value of β after the thin film has been fabricated on to the sub-
strate surface. Among the various techniques available, the most accurate
and direct method would be to use a small shock tube (ref. 13) and
measure the stagnation-point heat transfer at low shock Mach numbers
$(1.3 \leq M_{s,1} \leq 2)$. Then using the available theories for stagnation point
heat transfer (refs. 16 and 17), the value of β can be deduced very
easily. The details of the present calibration method are given in
appendix A. For quartz substrates, it has been well established that a
value of $\beta = 1512.5$ W-sec$^{1/2}$/m^2-k can be used. From the present calibration
data (given in appendix A), the value of β would be 1532.4 W-sec$^{1/2}$/m^2-k which
is about 1.3 percent more than the value assumed by other research workers.
Since the standard deviation between repeated runs in the present
calibration (Appendix A) is about 2.5 percent, it was decided to use the
value of $\beta = 1512.5$ W-sec$^{1/2}$/m^2-k in the present investigation.

BLUNT NOSE-CONE MODELS

Two $40°$ and $30°$ semivertex angle cone models with a spherical blunt
nose (6.35-mm radius) were fabricated out of stainless steel. The
geometrical details of these models are shown in figure 5. Quartz
substrates of 6.35 mm × 6.35 mm cross section were fitted in a slot cut
along a single ray in the conical portion of the models as shown in
figure 5. The top surfaces of the quartz substrates were optically
ground and polished to match the varying curvature along the cone surface.
About 14 to 16 thin-film gages at intervals of 3.2 mm were fabricated on the
quartz substrate as shown in figure 5. Photographs of the $40°$ cone model
with quartz substrate and thin films before and after the run are shown
in figures 6 and 7, respectively. The models were tested in the expansion
tube facility at zero and positive angles of attack with air as well
as helium test gas. The acceleration gas was the same as the test gas
in all the runs. The initial conditions used in the intermediate and
acceleration sections, as well as the different angles of attack used
in all the runs, are given in table III. All the thin films were damaged
by the fragments of secondary diaphragm during each run. Small white
fragments sticking to the gage substrate are visible in figure 7. The
performance of the thin film was not affected during the first 1/2 to 1
millisec time duration since the secondary diaphragm fragments arrived
at the model after about 1 millisec which was confirmed by monitoring
the gage response for a few millisecs during the run.

HEAT-TRANSFER MEASURING TECHNIQUES

The heating-rate distributions over cone models were measured
simultaneously by using two methods which are completely independent and
different from each other. Some important details of these methods are
given below (more details in appendices B and C).

Heating Rates Obtained by Numerical Integration

The surface-temperature time history of the gage substrate material (quartz) was measured by using an electric circuit to determine gage resistance (details given in appendix C) and the heating rate was deduced by numerical integration of surface temperature history. The relationship between the heat transfer per unit area per unit time $q(t)$ and an arbitrary surface-temperature history $\Delta T(t)$ with $\Delta T(0) = 0$, is (ref. 18):

$$q(t) = \frac{\sqrt{\pi\beta}}{2}\left\{\frac{\Delta T(t)}{\sqrt{t}} + \frac{1}{\pi}\int_0^t \frac{(\lambda/t)^{1/2}\Delta T(t) - \Delta T(\lambda)}{(t - \lambda)^{3/2}}\,d\lambda\right\} \tag{1}$$

$\beta = (k\rho c_p)^{1/2}$ for the quartz substrate and λ is a dummy variable.

Equation (1) has been modified for easy integration in reference 19 and that expression was used for the numerical integration. The surface-temperature time histories, measured by using the electric circuit (appendix C), were recorded and stored in the waveform recorder and then numerically integrated in a desktop calculator. More details are given in a later section.

Heating Rates Obtained by Electric Analog Network

In the derivation of the expression given in equation (1), several approximations are made (for details, ref. 18 may be referred). The numerical integration of equation (1) has to be performed in each case and this requires accurate surface-temperature data at very close intervals of time. In the early sixties, Skinner (ref. 20) and Meyer (ref. 21) independently realized that electrical analogs of a heat-conducting slab could be constructed which, if driven by a voltage proportional to surface temperature, would yield a signal proportional to the heat-transfer rate. This electric analog not only avoids the tedious numerical integration procedure but also avoids the assumptions made in arriving at the expression for heat-transfer rate given in equation (1). Furthermore, numerical integration of surface-temperature history can give erroneous values of $q(t)$ if very accurate values of measured $\Delta T(t)$ are not used at very close intervals of time. The basic principles of electric analog network and the actual circuit diagram used are given in appendix B. The relation between heating rate, the analog parameters, and substrate properties is given as:

$$q(t) = \frac{2V_a(t)}{aE_oD}\frac{\beta}{\sqrt{RC}} \tag{2}$$

$V_a(t)$ is measured as an output from the analog and all others are known constants defined in appendix B. Hence, $q(t)$ is directly proportional to $V_a(t)$. In the present investigation 10 channels of electric analog networks were designed and built; and these were used to measure directly the heating rates. The outputs from the analog channels were recorded and stored in the waveform recorder and the heating rates were directly printed out and plots were made using a desktop calculator.

Data Recording and Processing

Heat-transfer measurements over the cone surface were made with cone models mounted in the expansion tube test section (model nose located at 38 mm from the acceleration tube exit) with helium and air as the test gases. The initial flow conditions that were used are tabulated in table III.

For some of the runs the heat-transfer rates for all the gages on the cone surface were deduced from the measured surface temperatures by numerical interation. The surface temperatures were recorded using an electric circuit described in appendix C. Since this circuit had no preamplifier, the signal was amplified by using a differential amplifier. Proper ground connections to isolate ground loops were essential to avoid noise in the surface-temperature histories. The amplified signals were recorded on oscilloscopes as well as in the waveform recorder at 2.5-μsec intervals in all the runs using 15 out of 17 available channels. After each run, the stored data were transferred to a desktop calculator and printout of the data as well as plots was obtained. The data were also stored in a floppy disk and used for numerical integration to obtain the heat-transfer rate. One of the 15 channels in the waveform recorder was used to record the pitot pressure measured by a pressure transducer mounted at the blunt nose, as shown in figure 5. By using the proper calibration factor for the pressure gage, the printout from the calculator as well as the plots was obtained in actual pressure reading (either in psi or N/m^2).

For some runs, the heat-transfer rates were directly measured by using electric analog networks (details in appendix B). Since the circuit used in this case contained an amplifier in addition to the analog network, the signal output from the analog was directly recorded on oscilloscopes as well as in the waveform recorder, without any further amplification. In this case also, the data were recorded at 2.5-μsec intervals and processed in the calculator, since the number of analog network channels was only 10; the remaining 4 to 5 gages on the model were connected through the electric circuit (appendix C) and heating rates were obtained from the recorded surface temperatures by numerical integration. However, for the data obtained from analog networks, by using a proper constant (obtained from eq. (2)), the heating rates were directly printed out and plotted. Typical plots of surface temperatures and heat-transfer rates are shown in figure 8.

11

Data Reduction Procedure

Comparison of heating rates measured by analog network and deduced from numerical integration.- Two types of tests were made to compare the two different methods that have been used in the present analysis for heat-transfer measurements. First, the surface-temperature history obtained due to incident shock heating in air in the acceleration section was recorded by installing a thin-film gage inside the shock-tube wall. The surface-temperature history was recorded on a scope and the same signal was simultaneously fed into the analog network and the output from the analog was measured in the wave-form recorder. The surface-temperature history was measured from the oscilloscope film using a digitizer and the heating rates obtained by this procedure and those directly measured from the analog are compared in figure 9. The significant and important observation is that the numerical integration technique does not seem to simulate the fast response of the heating rate immediately behind the shock wave whereas the analog circuit shows a much better response in this region. About 35 to 40 μsecs after the shock passage, the two methods agree within 8 percent.

The heating rates were also deduced using the preceding procedure in the case of stagnation-point heating-rate measurement to a spherical nose of 25.4-mm radius mounted in the expansion tube test section. The test gas was helium and the other conditions correspond to run number EC 1500 given in table III. The surface-temperature history was recorded in the recorder at 2.5-μsec intervals. The numerical integration was performed by using data at two time intervals, namely 2.5 and 5.0 μsecs. The heating rates variation with time is shown in figure 10. The differences in heating rate by using the two time intervals is negligible. However, the computer time required to perform the integration over a 200-μsec time period was reduced by 50 percent for 5-μsec time intervals. The heating rate obtained from the analog network by feeding the same surface temperature was also recorded in the recorder at 2.5 μsec intervals and is compared in figure 10 with the values obtained by numerical integration. In this case also, the numerical integration does not seem to simulate the fast response of the heating rate immediately behind the shock wave. The two methods agree well (differences within 3 to 4 percent, except for a couple of peak values) after an elapsed time period of about 90 to 95 μsecs. This fact was taken into account in the data-reduction procedure adopted for the heating rates over cone models.

Heating-rate distributions over cone models.- The measured heating rates over the cone models ideally should remain constant with time. This ideal situation requires that the free-stream flow quantities are constant with time during the testing period. However, due to several nonideal effects that exist in the operation of the expansion tube facility, the free-stream flow quantities do exhibit some variation with time, especially in the case of helium test gas. Therefore, a time-averaging procedure was adopted to obtain the measured heating rates over the cone models.

12

As discussed earlier, the three required free-stream quantities, namely, wall-static pressure, pitot pressure, and the flow velocity are measured in each run and these are used as inputs to compute the theoretical heating-rate distribution. Therefore, it is important to obtain a consistent, time-averaged set of measured free-stream flow conditions. For every run, the variation of pitot pressure with time was plotted from the recorded data. The wall static pressure was read from the oscilloscope film in a digitizer and plots were made. The measured heating rates for two gage locations (generally in the beginning and toward the end of the quartz substrate) are also plotted. Typical plots are shown in figure 11. All three plots are matched with time t = 0 and then a common time interval was located in all three plots, during which period the flow quantities variation with time is minimum, as indicated in figure 11. In selecting this time interval, care is taken such that the initial period from t = 0 to the beginning of the time interval is at least 80 to 90 µsecs, especially in the case of numerical integration, in order to avoid the period of sluggish response as already discussed. One exception to this general rule has been made in the case of helium, due to nonavailability of better time intervals. This specific case has been noted in the discussion of results. After selecting the proper time interval, the pitot and static pressures were time-averaged. These values, along with the corresponding measured flow velocity for all the runs, are listed in table IV. The other flow quantities obtained from the computer program of reference 11, are listed in table V for all the runs. The heating rates were also time-averaged during the same time interval and the resulting heating-rate distribution along the length of the cone was obtained for all the runs.

THEORETICAL HEATING-RATE DISTRIBUTIONS OVER BLUNTED CONES

Theoretical heating-rate distributions have been obtained by using the method developed by Kumar and Graves (ref. 2) for the viscous flow over blunted cones at zero and small angles of attack. This method uses time-dependent viscous-shock-layer-type equations to describe the flow field between the body and the shock wave. A time-dependent finite-difference technique is used to solve the equations in the planes of symmetry of the flow field. Complete details of this method are given in reference 2.

Although the above analysis provides solutions at small angles of attack also, it is shown by Kumar et al (ref. 22) that a spherically blunted cone at small angles of attack can be replaced by equivalent cones at zero angle of attack for the purpose of calculating the shock shapes, surface pressure, skin friction, and heating rates. As an example, a 50° sphere cone at 5° angle of attack can be replaced by a 55° sphere cone at zero angle of attack on the windward side and a 45° sphere cone at zero angle of attack on the leeward side. This approach is used in the present investigation to obtain theoretical results for comparison with the measured heating rates at angles of attack.

In the present investigation, heating rates over the 30° and 40° sphere cones are computed under perfect-gas approximation for helium test gas and under chemical-equilibrium approximation for air-test gas. The viscosity for helium is obtained by the expression

$$\mu = 3.92 \times 10^{-7} T^{0.7} \text{ N-sec/m}^2 \tag{3}$$

where T is in $^{\circ}$K.

The equilibrium mass fractions of various species of air are computed by using the free-energy-minimization technique and their enthalpies are obtained by using the expressions given in reference 23. The flow properties predicted by this method agree within 1 percent from those predicted by the computer code of reference 11 at the stagnation point. The transport properties for equilibrium air are taken from reference 24.

The radiative-heating terms were also included in the governing equations. The radiative heat flux model used was that given in reference 25. In all the cases computed, it was found that the radiative heating rate was almost negligible.

The heating rates for the present experimental conditions were kindly computed by Dr. Ajay Kumar, Research Assistant Professor, Dept. of Mechanical Engineering and Mechanics, Old Dominion University, Norfolk, Virginia.

RESULTS AND DISCUSSION

Heat-Transfer Rate Distributions Over Cones in Helium Test Gas

The measured heating rates in helium test gas are compared with theoretical values for both the cone models in figures 12-15. The measured heating rates for the 40° cone at zero angle of attack are compared with theory in figure 12. As discussed earlier, the velocity obtained from the pressure film data between stations 27 and 31 (given in table I) was used for the theoretical computations; the other free-stream quantities were the same for both the cases. It is apparent from figure 12 that the theoretical computation using velocity obtained from pressure film data agrees with the measured values within 6 percent. The measured heating rates for 30° cone at zero angle of attack shown in figure 13 also agree with theory (within 7 to 8 percent) obtained by using U_{27-31}. However, in this case the measured heating rates are generally lower than the theoretical values. This may be due to the fact that the measured heating rates in this case were time averaged in a time interval which starts about 55 μsecs from the

beginning of the run, which may have affected the accuracy of numerical integration (as mentioned earlier). In figure 14, the heating rates measured over the 30° cone at zero angle of attack (a repeated run) seem to agree with theoretical values corresponding to a velocity (U_∞) 10 percent more than the one deduced from pressure film data (table I). The measured heating rates on the leeward side of 30° cone at +8° angle of attack are compared with theory in figure 15. The agreement is quite good in the early portion of the cone surface, but in the aft portion, the agreement is within 10 percent. This is probably due to a little more noise in the measured surface temperatures (toward the aft portion of the cone) than normally existed in other runs. Considering the uncertainty in the measured flow velocity, the agreement of the measured heating rates over both the cones with theory is considered satisfactory.

Heat-Transfer Rate Distributions Over Cones in Air Test Gas

The measured heating rates in air test gas are compared with theoretical values for both the cone models in figures 16-20. In figure 16, the measured heating rates over the two cones at +12° angle of attack (with gages on leeward side) are given. The theoretical value for 40° cones are about 5 to 6 percent more than the measured values in the beginning and 6 to 8 percent less toward the end of the cone. However, no theoretical values were available for 30° cones. In figures 17 and 18, the measured heating rates over 30° and 40° cones at zero angle of attack are compared with theory. The measured stagnation-point heating rate using a spherical blunt-nose model (0.0254-m nose radius) in a repeated run is also compared with theory in figures 17 and 18. The measured stagnation-point heating rates agree with theory within 2 percent. However, the measured heating rates over the cone surface for both the models are consistently higher than the computed values. the differences being 5 to 15 percent in the beginning and increase to as much as 80 percent toward the end of the cone surface. In figures 19 and 20, the measured heating rates at +4° angle of attack with gages on the windward side, are consistently much more (between 15 to 60 percent) than the computed values. The measurements, which are believed to be accurate to about 5 percent (appendix D) thus disagree with the computation by too much to attribute to measurement accuracy. At present no reasonable explanation exists for this discrepancy. It is observed from figures 16-20, that the discrepancy between theory and measurements increases as the effective cone angle increases.

CONCLUDING REMARKS

Heating-rate measurements over spherically blunted cones have been made in the expansion tube facility using air and helium test gases. The agreement between theory and measurements in the case of helium test gas is satisfactory. In the case of air test gas, the measured stagnation-point heating rate agrees with theory within 2 percent, but the measured heating rates over the cone surface on both the cone (40° and 30°) models are consistently higher than the theoretical values. The discrepancy between calculation and experiment increased as the local surface angle of attack increased. The reason for the discrepancy is not presently known.

APPENDIX A

CALIBRATION OF HEAT-TRANSFER GAGES

The quartz substrate's physical properties parameter $\beta[\beta = (k\rho c_p)^{1/2}]$ was determined by measuring the stagnation-point heat-transfer rate to a 0.0254-m radius spherical model mounted inside a calibration shock tube. A thin-film (palladium) heat-transfer gage was fabricated near the stagnation point using the same method as the one used for the heating-rate measurements over blunt cones in the expansion tube facility. The temperature coefficient of resistance for this gage was measured using the same procedure as was used for other gages. The value of α for this gage was 0.0024612 Ω/Ω K.

The calibration shock tube consists of a driver tube (0.914-m long and 0.078 mID) and a driven tube (1.829-m long and 0.154 mID) joined by a 0.305-m long transition piece at the diaphragm station. A polyester film diaphragm of 20-μm thickness was used. A shock wave of $M_{s,1} \cong 1.5$ was created by using helium as the driver gas and air at $p_1 = 160$ torr as the test gas in the driven tube. The shock speed was evaluated by measuring the time of arrival of the shock wave given by a counter reading which was started and stopped by shock tube wall pressures sensed by two pressure transducers mounted at 0.5336 m apart towards the end of the driven tube. The wall pressures which were used to trigger the counter were also monitored in an oscilloscope. The scopes were calibrated for gain factor as well as for sweep rate. The pressure transducers were calibrated using a pressure pulse generator. The shock speed was also deduced from the measured pressure ratio (p_2/p_1) as well as from the pressure film data. The accuracy of each method is discussed later in this appendix. The output from the stagnation-point heat-transfer gage was fed into an analog network (appendix B) and the output from the analog was measured on an oscilloscope. The gain factor for the analog was set at 100 and the initial voltage across the gage, E_0, was set at 1 volt.

The theoretical expression for the stagnation-point heat-transfer rate is given by reference 16:

$$q_{st} = 0.763 P_r^{-0.6} (\rho_e \mu_e)^{1/2} (U_2/R_n)^{1/2} \left[\frac{R_n}{U_2} \frac{dU_e}{dS} \right]^{1/2} \tag{1-A}$$

where the Prandtl number $P_r = 0.71$ for air at low temperatures. Since the flow velocity U_2 behind the incident shock wave $M_{s,1}$ is subsonic in the present case an appropriate nondimensional velocity gradient $\frac{R_n}{U_2} \frac{dU_e}{dS}$ given in reference 17 has to be used. The subsonic flow velocity U_2 is the free-stream velocity for the spherical model. Equation (1-A) can be expressed as a function of flow Mach number $M_2 (M_2 = U_2/a_2)$ and $(p_1/R_n)^{1/2}$ where p_1 is the initial pressure in the driven tube and R_n

16

is the model nose radius. The variation of the parameter $q_{st}\sqrt{R_n/p_1}$ with flow Mach number M_2 is shown in figure 1-A.

The stagnation-point heating rate was measured at an initial pressure of 160 torr in the driven tube and the incident shock Mach number $M_{3,1}$ was around 1.55. The same condition was repeated several times and an average value of β was deduced from these repeated runs. The procedure for deducing β is illustrated here for a single run and all the data obtained in the repeated runs are tabulated in this section. Run No. 11, $p_1 = 160$ torr; $R_n = 0.0254$ m; analog output measured from scope: 10.29 mv; room temperature: $25^\circ C$; speed of sound $a_1 = 346.37$ m/sec. Time interval measured by counter: 981 µsecs. $U_{s,1} = 543.9$ m/sec. $M_{s,1} = 1.57$, $M_2 = 0.66$ from charts.

From figure 1.A:

$$q_{st}\,(R_n/p_1)^{1/2} = 2.4 \times 10^4 \text{ watts/m}^2. \tag{2-A}$$

From the analog heat-transfer relation (appendix B)

$$q_{st} = \frac{\beta}{\alpha}\frac{2V_a}{DE_o}\frac{1}{\sqrt{RC}} ;$$

$\sqrt{RC} = 1.975 \times 10^{-3}$ sec$^{1/2}$ for the analog circuit.

$E_o = 1000$ mv

$D = 100$; $\alpha = 0.0024612$ Ω/Ω K,

with the measured value of $V_a = 10.29$ mv,

$$q_{st} = 1.042 \times 10^{-1}(\beta/\alpha) \tag{3-A}$$

Equating (2-A) and (3-A) gives

$$(\beta/\alpha) = 5.7807 \times 10^5 \quad \text{and} \quad \beta = 1422.74 \; W\sqrt{t}/m^2 \, {}^{\circ}K.$$

The difference from the assumed value of 1512.5 is -5.9340 percent.

The shock speed $U_{s,1}$ was also deduced from the wall-pressure film data and gives a shock Mach number $M_{s,1}$ of 1.575, and the corresponding flow Mach number M_2 is 0.665 from charts. The value of $q_{st}\sqrt{R_n/p_1}$ from figure 1-A is 2.45×10^4. Then the β value deduced from the equations already given is 1452.3 which is 3.97 percent less than the assumed value of 1512.5.

Since the pressure p_2 behind the shock wave was also measured, the shock Mach number $M_{s,1}$ was also inferred from the pressure ratio p_2/p_1 from charts. In this case, pressure behind the shock wave would be $p_2 = 5.56 + 3.0947 = 8.6547$ psi and $p_1 = 3.095$ psi. Hence, $p_2/p_1 = 2.797$. Then $M_{s,1} = 1.59$ from charts. The corresponding M_2 is 0.68 and $q_{st}\sqrt{R_n/p_1} = 2.6 \times 10^4$ from figure 1-A. Then the β value would be 1541.27 which is 1.9 percent more than the assumed value of 1512.5. The β values deduced by using the preceding method for five repeated runs are tabulated below.

$$p_1 = 160 \text{ torr}, \; E_o = 1000 \text{ mv}, \; D = 100, \; \alpha = 0.0024612 \; \Omega/\Omega \, K$$

RUN NUMBER		$M_{s,1}$	M_2	$q_{st}\sqrt{\dfrac{R_n}{p_1}}$	q_{st} (watts/m^2)	V_a (mv)	(β/α)	$\dfrac{\beta}{W\sqrt{t}/m^2K}$	% diff
1	1*	1.568	0.660	2.4×10^4	6.023×10^4	↑	5.947×10^5	1463.7	-3.2
	2	1.582	0.672	2.52×10^4	6.32×10^4	10.0	6.24×10^5	1535.5	+1.54
	3	1.585	0.672	2.52×10^4	6.32×10^4	↓	6.24×10^5	1545.8	+1.54
3	1	1.578	0.665	2.45×10^4	6.149×10^4	↑	5.643×10^5	1388.8	-8.2
	2	1.602	0.690	2.70×10^4	6.776×10^4	10.76	6.219×10^5	1530.6	+1.2
	3	1.595	0.685	2.65×10^4	6.651×10^4	↓	6.104×10^5	1502.3	-0.67
9	1	1.565	0.655	2.35×10^4	5.898×10^4	↑	5.430×10^5	1335.3	-11.7
	2	1.575	0.665	2.45×10^4	6.149×10^4	10.74	5.656×10^5	1392.1	-7.96
	3	1.610	0.695	2.80×10^4	7.028×10^4	↓	6.46×10^5	1591.1	+5.2
10	1	1.574	0.662	2.450×10^4	6.149×10^4	↑	5.50×10^5	1353.7	-10.5
	2	1.583	0.672	2.520×10^4	6.325×10^4	11.04	5.567×10^5	1392.4	-7.9
	3	1.605	0.690	2.700×10^4	6.776×10^4	↓	6.061×10^5	1491.7	-1.4
11	1	1.570	0.660	2.400×10^4	6.023×10^4	↑	5.778×10^5	1422.2	-5.97
	2	1.575	0.665	2.450×10^4	6.149×10^4	10.29	5.901×10^5	1452.3	-3.97
	3	1.590	0.680	2.600×10^4	6.525×10^4	↓	6.262×10^5	1541.3	+1.90

*1: $M_{s,1}$ deduced from counter reading

2: $M_{s,1}$ deduced from wall pressure film

3: $M_{s,1}$ deduced from measured shock pressure ratio

Average value of β from five runs deduced from shock pressure ratio (item 3 in the table) is 1532.4 $W\sqrt{t}/m^2K$, which is 1.3 percent more than the assumed value of 1512.5. Standard deviation from run to run in the case of 3 is 2.5 percent from the mean value.

APPENDIX A

From the three preceding methods of obtaining the shock speed, it is apparent that by using the measured pressure ratio across the shock wave would result in better agreement with the value of β already used by other investigators. In order to eliminate the possibility that this may be an isolated single case, the same run was repeated 5 times and the same trend exists consistently in all the repeated runs as shown in the preceding table. The shock speed deduced by counter reading is probably affected by two factors: the trigger sensitivity of the counter (may not be exactly same for both start and stop gates) and the initial speed of sound a_1 which was computed by using the outside room temperature which may not be the same as the gas temperature inside. For the case of shock velocity deduced from the wall pressure film data, the probable error from the counter is avoided, but the error due to incorrect initial temperature still affects the deduced shock Mach number. In the case of shock velocity deduced from the measured pressure ratio (p_2/p_1), both errors are avoided. In this case, we depend on only the initial pressure p_1 which is measured accurately using an absolute vacuum gage and the pressure transducer was calibrated using a pressure-pulse generator.
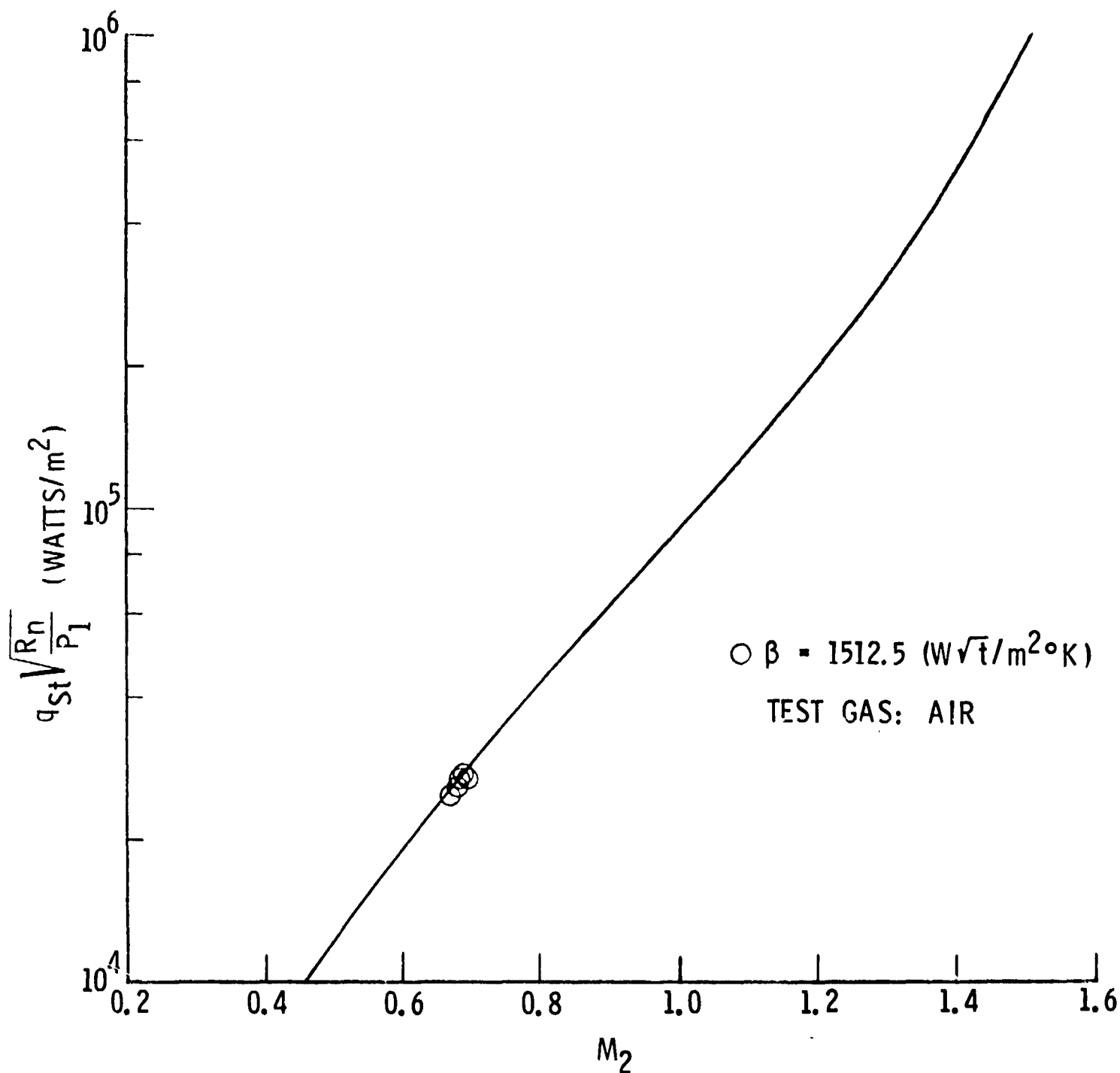
10^6

10^5

$q_{St}\sqrt{\dfrac{R_n}{P_1}}$ (WATTS/m^2)

10^4

$\bigcirc \ \beta = 1512.5 \ (W\sqrt{t}/m^2 {}^\circ K)$

TEST GAS: AIR

0.2   0.4   0.6   0.8   1.0   1.2   1.4   1.6

M_2

Figure 1A.- Variation stagnation point heating rate with flow Mach
Number M_2.

20

APPENDIX B

ANALOG NETWORK

It was realized by Skinner (ref. 20) and Meyer (ref. 21) that electrical analogs of a heat-conducting slab could be constructed, which if driven by a voltage proportional to surface temperature, would yield a signal proportional to the heat-transfer rate. Some modifications to these basic circuits have been proposed in reference 13. The present analog circuit is essentially based on the modifications proposed in reference 13.

Analogy Between Heat and Current Conduction

The basis for constructing an electrical analog of a heat-conducting slab arises from the similar forms of the equations for heat conduction and diffusion of electrical charge in a system in which there is uniformly distributed resistance and capacitance. Because of the difficulty of constructing an electrical model with continuous variation of capacitance and resistance, it is usual to approximate this by employing a network of lumped constants. The heat-transfer gage substrate, which is assumed to be semi-infinite, may be considered to be consisting of a number of small strips of slabs of backing material. Each slab is considered as a capacitor and resistor. Surface-temperature change corresponds to the applied voltage to the network, the corresponding change of current in the network corresponds to the heat-transfer rate. The commonly used T-section network and the analogy between heat and current conduction are shown in figure 1-B. The current through the network is measured as a voltage drop V_a across the first resistance in the network. Then using the relation between the heat transfer and the current (fig. 1-B), an expression for heat-transfer rate can be derived as

$$q(t) = \frac{2V_a(t)}{E_o \alpha D} \left[\frac{k \rho c_p}{RC} \right]^{1/2} \tag{1-B}$$

For a given $q(t)$ the analog output voltage $V_a(t)$ is proportional to $(RC)^{1/2}$, whereas the response time of the analog circuit is given by RC so that, in general, it is necessary to make a compromise between fast response and adequate output signal level. The network must be made long enough so that over the time during which measurements are being made, the system behaves as though it were semi-infinite.

Circuit diagram of analog network and the preamplifier is shown in figure 2-B. It consists of 30 RC units with 10 kΩ and 390 pf as resistance and capacitance in each RC unit, respectively. The first five RC units are made of components which are of 5-percent accuracy. This will ensure accurate voltage measurement across the first resistance. With R and C values used, the response time is 3.9 µsecs and the analysis of reference 13 shows less than 0.1-percent error due to finite length of network.

APPENDIX B

The preamplifier in figure 2-B consists of a constant current source and a voltage amplifier with a maximum gain of 100. The signal, amplified through the amplifier, is directly fed to the analog network, but the same signal is attenuated by 10 times and measured as T-out which is the surface temperature response of the gage. The gain adjust is a precision 10-turn potentiometer which can be used to set the gain at any value from 1 to 100. The gain corresponds exactly to the value set on the gain adjust potentiometer. The current adjust potentiometer is used to set any desired current level through the thin film and two binding posts are provided to measure the initial voltage across the thin film. The maximum limit of voltage change across the thin film should not be more than about 100 to 150 millivolts during the test region of any run to avoid saturation in the amplifier. This can be maintained by properly setting the current level through the gage.

22

ANALOG NETWORK
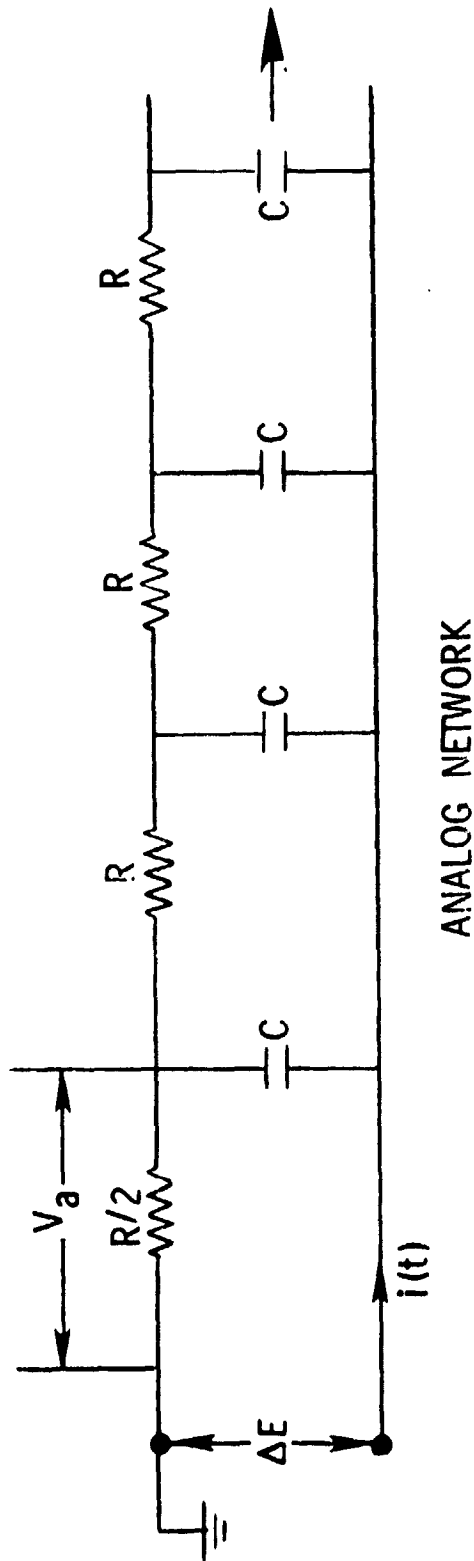
HEAT CONDUCTION EQUATION

$$\left(\frac{\partial T}{\partial t}\right) = \left(\frac{K}{\rho C_p}\right)\left(\frac{\partial^2 T}{\partial X^2}\right)$$

HEAT TRANSFER

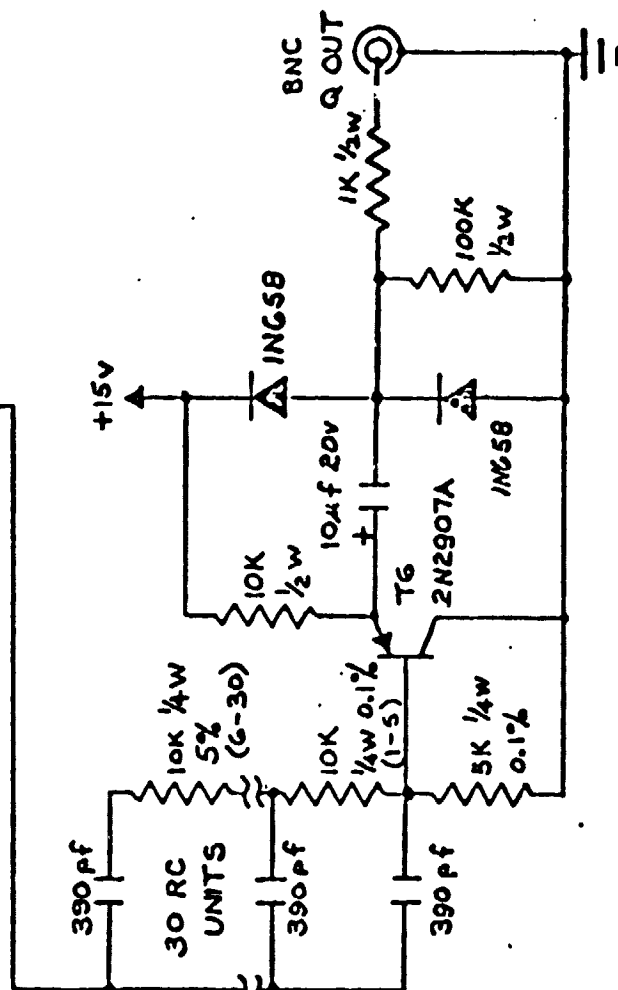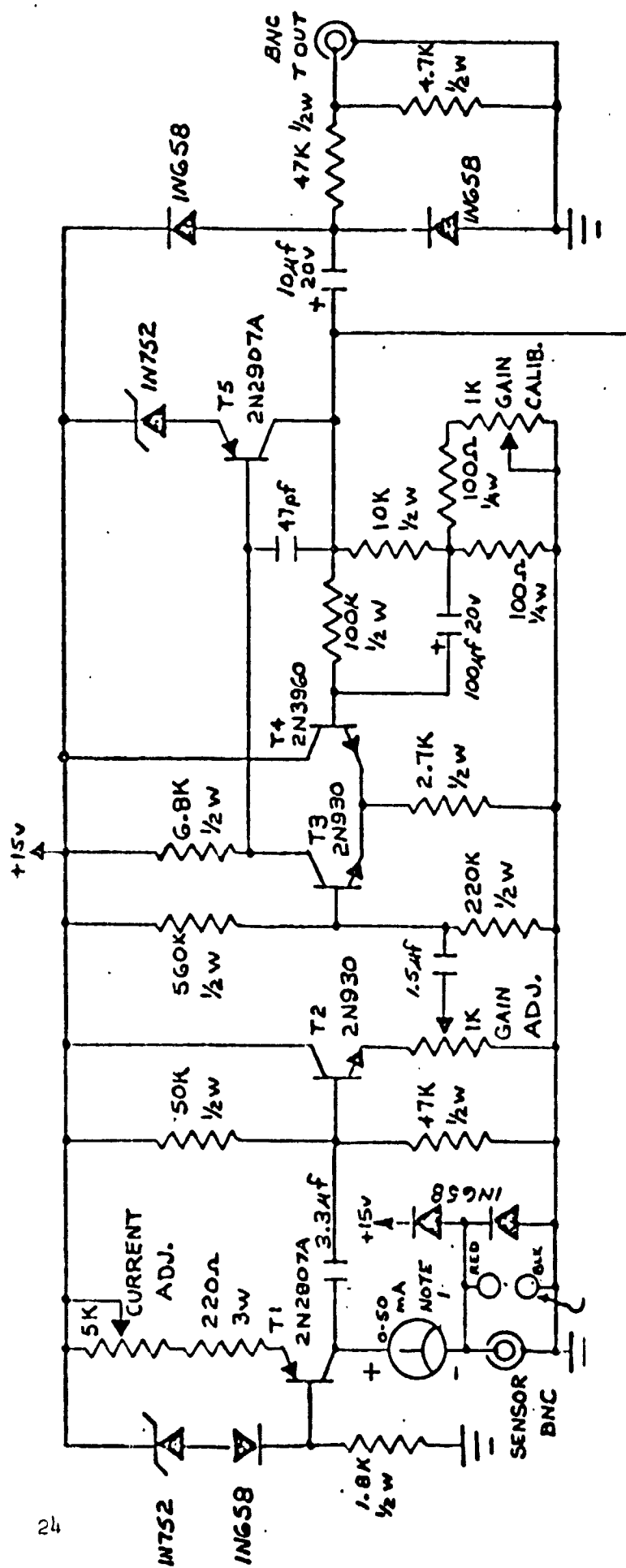$$q(t) = (K)\left[\frac{\partial T(X,t)}{\partial X}\right] X = 0$$

$$= \left[\frac{1}{\alpha, E_0}\right]\sqrt{\frac{R}{C}}\sqrt{(K\rho C_p)}\;[i(t)]$$

ELECTRICAL CONDUCTION EQUATION

$$\left(\frac{\partial E}{\partial t'}\right) = \left(\frac{1}{RC}\right)\left(\frac{\partial^2 E}{\partial X'^2}\right)$$

CURRENT

$$i(t) = \frac{1}{R}\left(\frac{\partial E(X't')}{\partial X'}\right) X' = 0$$

$$i(t) = \frac{2V_a}{R}$$
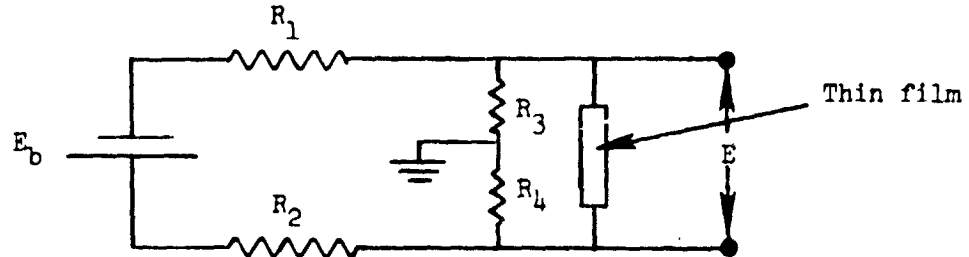
Figure 1B.- Analogy between heat and current conduction.

23

Figure 28.- Circuit diagram of analog network.

24

ELECTRIC CIRCUIT USED TO MEASURE SURFACE-TEMPERATURE HISTORY

The electric circuit used is shown in the sketch given below.

Let $(R_1 + R_2) = R_b$.

Assumptions:

    1. R_3 and $R_4 \gg R_b \gg R$

    2. Temperature coefficient of resistance of thin film α is constant. The change in resistance of the thin film at any instant during a run, ΔR, is given by

$$\Delta R = (R - R_o) = R_o\alpha(T - T_o) = R_o\alpha\Delta T$$

or

$$\Delta T = \Delta R/(\alpha R_o) \tag{1-C}$$

where quantities with subscript 0 are initial values at $t = 0$; $(\Delta R/R_o)$ can be determined from the given quantities R_o, R_b, E_o and the measured change in voltage across the thin film during a run. From the circuit shown above, the following relations hold;

$$\Delta E = (E - E_o) \tag{2-C}$$

$$\therefore$$

$$E_o = \frac{R_o E_b}{R_o + R_b} \equiv I_o R_o \tag{3-C}$$

$$E = IR \equiv \frac{RE_b}{R + R_b} \tag{4-C}$$

where E_b is the battery voltage.

From equations (2-C), (3-C), and (4-C) we have

$$\Delta E = E_b \left[\frac{R}{R + R_b} - \frac{R_o}{R_o + R_b} \right] \tag{5-C}$$

Using relation given in equation (3-C), equation (5-C) can be written as:

$$\frac{\Delta R}{R_o} = \frac{\Delta E}{E_o} \left[\frac{1 + E_o/(E_b - E_o)}{1 - \{E_o/(E_b - E_o)\}\frac{\Delta E}{E_o}} \right] \tag{6-C}$$

Using equation (1-C), the change in surface temperature is given by,

$$\Delta T = \frac{\Delta E}{\alpha E_o} \left[\frac{1 - E_o/(E_b - E_o)}{1 - \{E_o/(F_b - E_o)\} \frac{\Delta E}{E_o}} \right] \tag{7-C}$$

ΔE is the measured change in voltage across the gage. E_o and E_b are the initial voltage across the gage and the battery voltage, respectively. The relation given in equation (7-C) was derived by Wilfred Friesen of Langley Research Center.

26

APPENDIX D

ERROR ESTIMATION IN HEAT-TRANSFER MEASUREMENT

To estimate the absolute error involved in measuring the heating rates, the principles outlined in reference 26 are used. Some of the important principles are noted below.

(a) All the errors are classified either independent or dependent.

(b) In the case of independent errors, the logical way of adding the separate contributions is to take the square root of the sum of their squares. This procedure is considered too conservative and some research workers reduce the total error, perhaps by one third.

(c) In the case of dependent errors, the rule is to replace the square root of the sum of squares addition by algebraic addition.

The heat transfers that were measured by using electric analog network (appendix C) were deduced by using the following expression

$$q = \frac{2V_a}{E_o \alpha D} \frac{\beta}{(RC)^{1/2}} \tag{1-D}$$

The error due to the finite length of the analog network is about 0.1 percent (appendix B) and the value of RC can be taken as quite accurate since the values of R and C in the network are of 0.1-percent accuracy. Then, the change in the heating rate can be written from equation (1-D) as

$$\frac{\Delta q}{q} = \frac{\Delta V_a}{V_a} + \frac{\Delta \beta}{\beta} - \frac{\Delta \alpha}{\alpha} \tag{2-D}$$

The error in measuring V_a by using the recording system is estimated to be less than 2 to 3 percent. The error in β can be taken as 2.5 percent (appendix A). The value of α of the thin film was obtained by normalizing with the resistance of the gage measured at ambient temperature during calibration. But the initial temperature of the thin film just before the run is made will be different since the ambient temperature will vary and in addition, the thin film gets heated due to constant current passing through the film. The error introduced due to these effects is taken conservatively as 3 percent.

Then

27

$$\frac{\Delta q}{q} = \sqrt{2.5^2 + 2.5^2 + 3^2} = 4.6 \text{ percent}$$

Thus, a conservative error estimate would be around 5 percent.

The heating rates deduced from numerical integration are subjected to the same errors as noted above, but an additional error in selecting the time integration steps is introduced. This additional error is shown to be negligible by selecting different time steps as noted elsewhere in this report.

REFERENCES

1. Fivel, H. J.; Masek, R. V.; and Mackapetus, L. J.: Analytical Comparison of Hypersonic Flight and Wind Tunnel Viscous/Inviscid Flow Fields, NASA Contractor Report, prepared by McDonnell Douglas Astronautics-East, St. Louis, Missouri.

2. Ajay Kumar and Graves, R. A. Jr.: Numerical Solution of the Viscous Hypersonic Flow Past Blunted Cones at Angles of Attack. AIAA paper No. 77-172, Jan. 1977.

3. Trimpi, Robert L.: A Preliminary Theoretical Study of the Expansion Tube, A New Device for Producing High-Enthalpy Short-Duration Hypersonic Gas Flows. NACA TRR-133, 1962.

4. Trimpi, Robert L.: A Theoretical Investigation of Simulation in Expansion Tubes and Tunnels. NASA TR-R243, 1966.

5. Jones, Jim J.; and Moore, John A.: Exploratory Study of Performance of the Langley Pilot Model Expansion Tube with a Hydrogen Driver. NASA TN D-3421, 1966.

6. Miller, Charles G. III: A Program for Calculating Expansion-Tube Flow Quantities for Real-Gas Mixtures and Comparison with Experimental Results. NASA TN D-6830, 1972.

7. Haggard, Kenneth V.; and Goad, William K.: A Comparison of Measured and Predicted Test Flow in an Expansion Tube with Air and Oxygen Test Gases. NASA TN D-8068, 1975.

8. Miller, C. G. III; and Wilder, S. E.: Program and Charts for Determining Shock Tube, Expansion Tube, and Expansion Tunnel Flow Quantities for Real Air. NASA TN D-7752, 1975.

9. Shinn, Judy L.; and Miller, Charles, G. III: Experimental Perfect-Gas Study of Expansion Tube Flow Characteristics, NASA Technical Paper 1317, 1978.

10. Moore, John A.: Description and Initial Operating Performance of the Langley 6-Inch Expansion Tube Using Heated Helium Driver Gas NASA TMX-3240, 1975.

11. Miller, C. G. III: Computer Program of Data Reduction Procedures for Facilities Using CO_2-N_2-O_2-Ar Equilibrium Real-Gas Mixtures, NASA TMX-2512, March 1972.

12. Miller, C. G. III; and Jones, Jim, J.: Incident Shock-Wave Characteristics in Air, Argon, Carbon Dioxide and Helium in a Shock Tube with Unheated Helium Driver, NASA TND-8099, 1975.

13. Walenta, Z. A.: Analog Networks for High Heat-Transfer Rate Measurements, UTIAS TN 84, Institute for Aerospace Studies, University of Toronto, Toronto, Canada, Nov. 1964.

14. Taylor, B. W.: Development of a Thin Film Heat Transfer Gage for Shock Tube Flows, UTIA TN 27, Institute for Aerospace Studies, University of Toronto, Toronto, Canada, June 1959.

15. Skinner, G. T.: A New Method of Calibrating Thin Film Gage Backing Materials, Report No. CAL-105, Cornell Aeronautical Laboratory Inc., Buffalo, N.Y., June 1962.

16. Fay, J. A. and Riddell, F. R.: Theory of Stagnation Point Heat Transfer in Dissociated Air, Journal of the Aeronautical Sciences, Vol. 25, No. 2, Feb. 1958, pp. 73-85.

17. Truitt, R. W.: Hypersonic Aerodynamics, The Ronald Press Company, New York, 1959.

18. Vidal, R. J.: Model Instrumentation Techniques for Heat Transfer and Force Measurements in a Hypersonic Shock Tunnel. WADC Technical Note 56-315 (AD-97238), Cornell Aero. Lab., Buffalo, N.Y. Feb. 1956.

19. Cook, W. J. and Felderman, E. J.: Reduction of Data from Thin-Film Heat Transfer Gages, A Concise Numerical Technique, AIAA Journal Vol. 4, No. 3, March 1966, pp 561-562.

20. Skinner, G. T.: Analog Network to Convert Surface Temperature to Heat Flux, CAL Report No. 100, Cornell Aeronautical Laboratory, Buffalo, N.Y., Feb. 1960.

21. Meyer, R. F.: A Heat-Flux-Meter for Use with Thin-Film Surface Thermometer, NRC Aero, Report LR-279, National Research Council, Ottawa, Canada, April 1960.

22. Ajay Kumar; Tiwari, S. N.; and Graves, R. A. Jr.: Effects of Small Angles of Attack on the Radiating Viscous Shock Layer Solutions for Jovian Entry, AIAA paper No. 78-909, 2nd AIAA/ASME Thermophysics and Heat Transfer Conference, May 1978.

23. Hansen, C. F.: Approximations for the Thermodynamic and Transport Properties of High Temperature Air, NASA TR-R-50, 1959.

24. Yos, J. M.: Transport Properties of Nitrogen, Hydrogen, Oxygen and Air to 30,000 K. Tech. Mem. RAD-TM-63-7, AVCO Corp. March 1963.

25. Ajay Kumar; and Jain, A. C.: Hypersonic Radiating Merged Shock Layer Near the Blunt-Body Stagnation Region, Inst. J. Heat and Mass Transfer, Vol. 17, pp. 197-204, 1974.

26. Beers, Y.: Introduction to the Theory of Error, Addison-Wesley Publishing Company, Inc., Cambridge, Mass. 1953.

TABLE I.- MEASURED FREE-STREAM VELOCITIES

Test gas: Air

Run number	Velocity at tube exit (from st.-line fit to the data)	Velocity between stations (27) and (31) (1.554 m)		
		From counter reading*	From HT film data	From pressure film data
	(m/s)	(m/s)	(m/s)	(m/s)
EC 1477	5061	5090	5096	5062
EC 1478	5092	5182	5062	5096
EC 1479	5130	5212	5215	5129
EC 1494	5114	5146	5215	5096
EC 1495	5176	5198	5251	5096
EC 1496	5157	5251	5378	5129
EC 1497	5203	5323	5341	5215
EC 1498	5026	5146	-	-

*Counters are triggered by heat-transfer gages.

Test gas: Helium

Run number	Velocity at tube exit	From counter reading	From HT film data	From pressure film data
EC 1473	6410	6396	6396	6787
EC 1475	6342	6242	6318	6847
EC 1476	6376	6267	6292	6728
EC 1491	6474	6318	6345	6787
EC 1499	6253	6252	-	-
EC 1500	6415	6267	6585	6670

Station locations: (27) : 19.732 m; (31) : 21.286 m; tube exit: 21.610 m.

Mid-point location between St. (27) and (31) : 1.1 m from tube exit.

TABLE II.- TYPICAL α VALUES FOR THIN-FILM GAGES

Gage number	Gage resistance at room temp. (24.4°C)	α values (Ω/Ω°K)			
		38.39°C	52.2°C	66.2°C	79.5°C
1	-	-	-	-	-
2	77.8(Ω)	0.002364	0.002373	0.002377	0.002367
3	76.9	0.002366	0.002373	0.002379	0.002368
4	76.4	0.002361	0.002367	0.002373	0.002363
5	77.7	0.002361	0.002366	0.002373	0.002363
6	78.8	0.002362	0.002366	0.002374	0.002364
7	80.5	0.002363	0.002369	0.002377	0.002367
8	81.9	0.002358	0.002367	0.002375	0.002366
9	83.7	0.002362	0.002370	0.002379	0.002370
10	94.6	0.002330	0.002310	0.002323	0.002315
11	84.8	0.002359	0.002370	0.002380	0.002370
12	83.2	0.002362	0.002372	0.002383	0.002373
13	83.5	0.002365	0.002370	0.002378	0.002369
14	83.6	0.002367	0.002369	0.002379	0.002370
15	82.6	0.002365	0.002366	0.002377	0.002372
16	87.6	0.002351	0.002372	0.002380	0.002371
Standard deviation (from the mean value)		0.4%	0.65%	0.6%	0.6%

TABLE III.- INITIAL TEST CONDITIONS

Run number	Test gas / Accel. gas	Semivertex cone angle deg	Angle of attack deg	P_1 (N/m^2)	P_{10} (N/m^2)	Remarks
EC 1473		30	+8			Gages on leeward side
EC 1475		40	0			——
EC 1476		30	0			——
EC 1491	He/He	30	0	689.5	16.0	——
EC 1499		-	-			}Stag. point heat
EC 1500		-	-			}transfer (R_n = 25.4 mm)
EC 1477		40	+12			}Gages on leeward side
EC 1478		30	+12			}
EC 1479		40	0			——
EC 1494		30	0			——
EC 1495	Air/Air	40	+4	3447	6.67	}Gages on windward side
FC 1496		30	+4			}
EC 1497		-	-			}Stag. point heat
EC 1498		-	-			}transfer (R_n = 25.4 mm)

TABLE IV.- MEASURED FREE-STREAM CONDITIONS

Test gas: Air

Run number	P_t (N/m^2)	$P_{\infty 2}$ (N/m^2)	T_w (°K)	q_{St}* (W/m^2)	U_{27-31} (m/sec)
EC 1477	108058	1684	325	—	5062
EC 1478	113747	1620	319	—	5096
EC 1479	116170	1606	356	—	5129
EC 1494	113800	1682	345	—	5096
EC 1495	111031	1722	359	—	5096
EC 1496	119102	1776	360	—	5129
EC 1497	—	2052	380	1.348×10^7	5215
EC 1498	—	2000	380	1.277×10^7	5026

Test gas: Helium

Run number	P_t (N/m^2)	$P_{\infty 2}$ (N/m^2)	T_w (°K)	q_{St}* (W/m^2)	U_{27-31} (m/sec)
EC 1473	52299	958	314	—	6787
EC-1475	51965	863	328	—	6847
EC 1476	49678	807	313	—	6728
EC 1491	51299	834	317	—	6787
EC 1499	—	815	333	7.69×10^6	—
EC 1500	—	963	330	8.3×10^6	6670

*Nose radius R_n = 0.0254 m for stagnation-point heating-rate measurements. R_n = 0.00635 m for blunt-nosed cone models (as shown in fig. 5).

TABLE V.- COMPUTED FREE-STREAM FLOW CONDITIONS (REF. 11)

Test gas: Air

Run number	Density (kg/m^3)	Temperature $(°K)$	Enthalpy (m^2/sec^2)	Compressi-bility	Specific heat ratio	Mach number	Reynolds number per meter
EC 1477	4.35×10^{-3}	1349	1.456×10^6	1.010	1.313	7.10	4.38×10^5
EC 1478	4.52×10^{-3}	1248	1.336×10^6	1.010	1.319	7.41	4.81×10^5
EC 1479	4.56×10^{-3}	1227	1.311×10^6	1.010	1.320	7.52	4.94×10^5
EC 1494	4.52×10^{-3}	1297	1.394×10^6	1.010	1.316	7.28	4.70×10^5
EC 1495	4.41×10^{-3}	1361	1.470×10^6	1.010	1.312	7.12	$4.45 \ 10^5$
EC 1496	4.67×10^{-3}	1325	1.428×10^6	1.010	1.314	7.25	4.82×10^5

Test gas: Helium

Run number	Density (kg/m^3)	Temperature $(°K)$	Enthalpy (m^2/sec^2)	Compressi-bility	Specific heat ratio	Mach number	Reynolds number per meter
EC 1473	1.277×10^{-3}	360	1.87×10^6	1.000	1.667	6.08	3.59×10^5
EC 1475	9.5×10^{-4}	331	1.72×10^6	1.000	1.667	6.39	3.75×10^5
EC 1476	1.235×10^{-3}	313	1.63×10^6	1.000	1.667	6.46	3.80×10^5
FC 1491	1.254×10^{-3}	318	1.65×10^6	1.000	1.667	6.46	3.84×10^5

Primary diaphragm
(single or double)

Secondary
diaphragm

Unsteady
expansion

Unsteady
expansion

Interface

Interface

Incident
shock

Incident
shock

(1) Quiescent test gas

(2) Test gas behind
     incident shock in
     intermediate section

(3) Driver gas following
     unsteady expansion

(4) Driver gas

(5) Test gas in acceleration
     section (free stream)

(10) Quiescent acceleration gas

(20) Acceleration gas behind
      incident shock in
      acceleration section

Driver
section

Intermediate
section

Acceleration
section

Time

Distance

Figure 1.- Schematic diagram of expansion tube flow sequence.
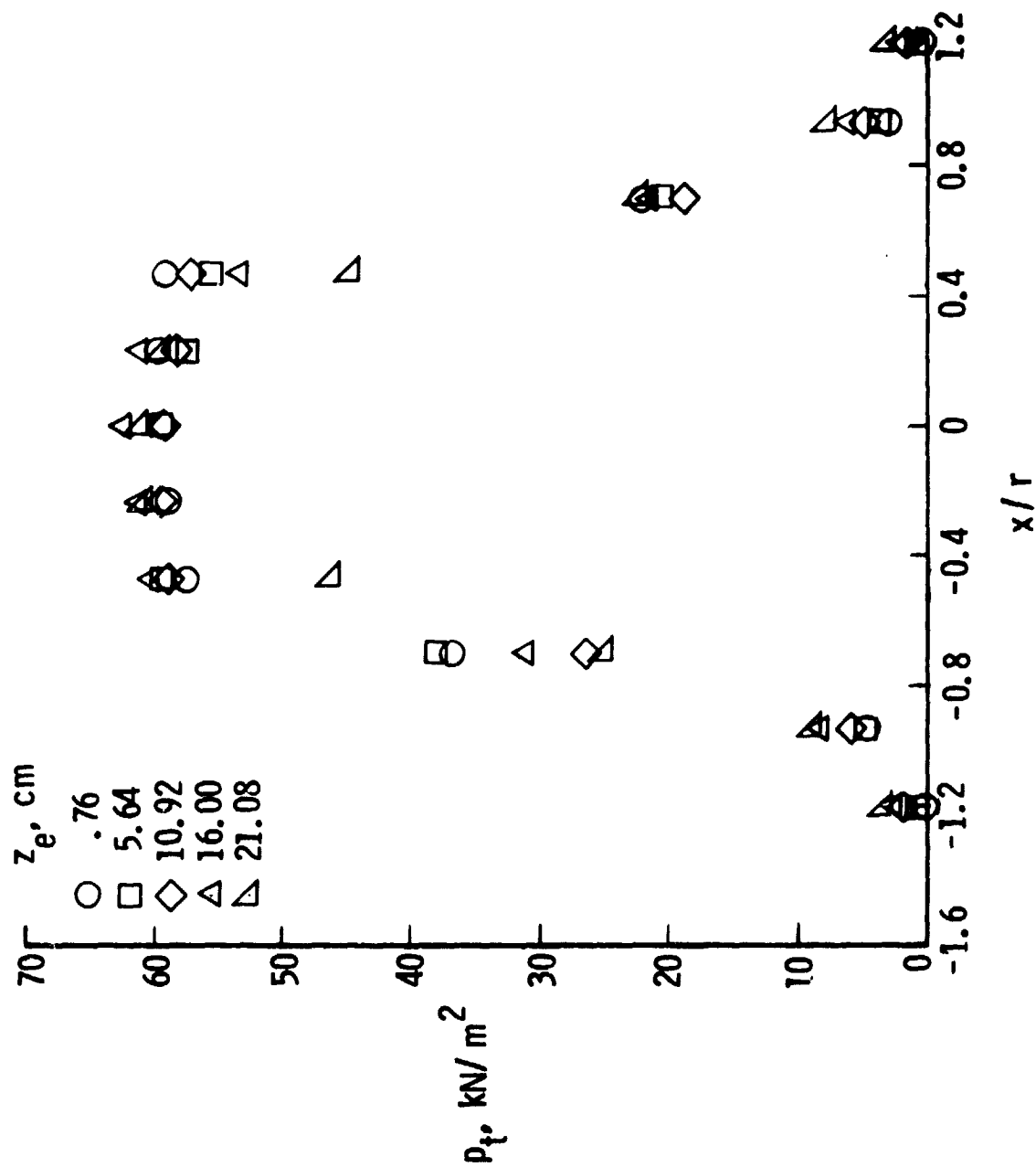
Figure 2.- Pitot-pressure profile at various distances downstream of tube exit. $p_1 \approx 3.45$ kN/m^2; $p_{10} \approx 16.00$ N/m^2; t = 200 μs.
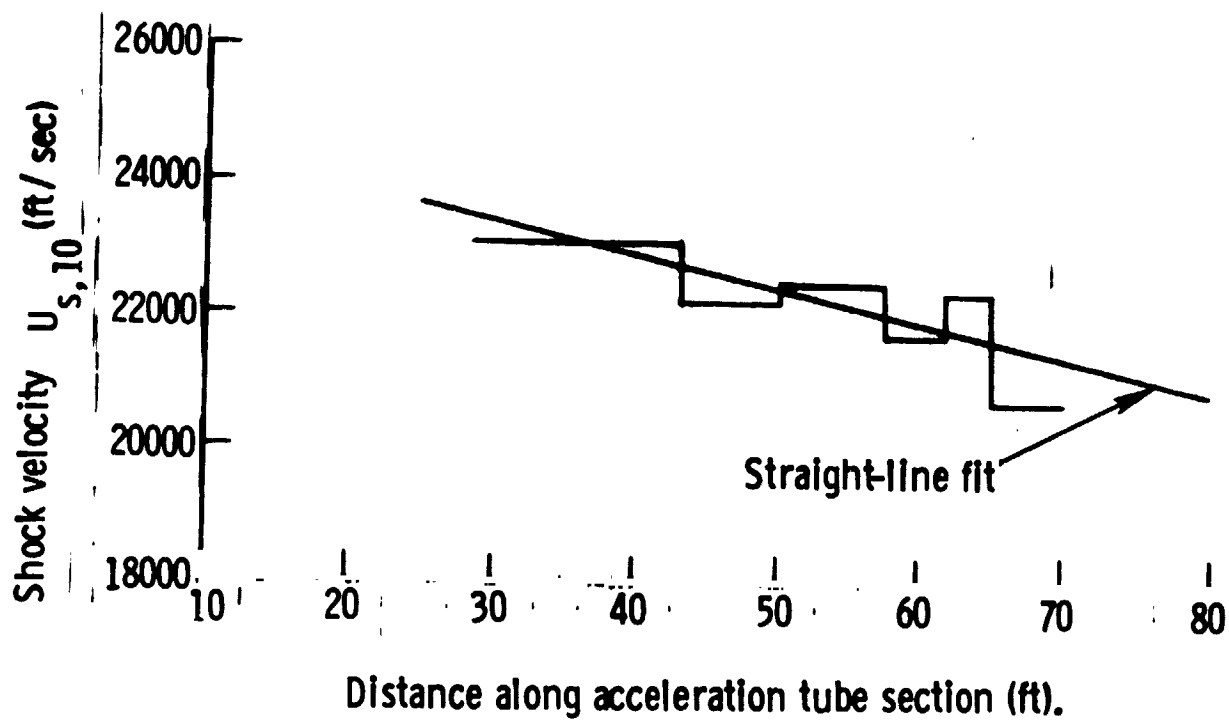
Figure 3.- Variation of shock velocity, $U_{s,10}$, along acceleration section. Test gas: Helium, Run 1491.
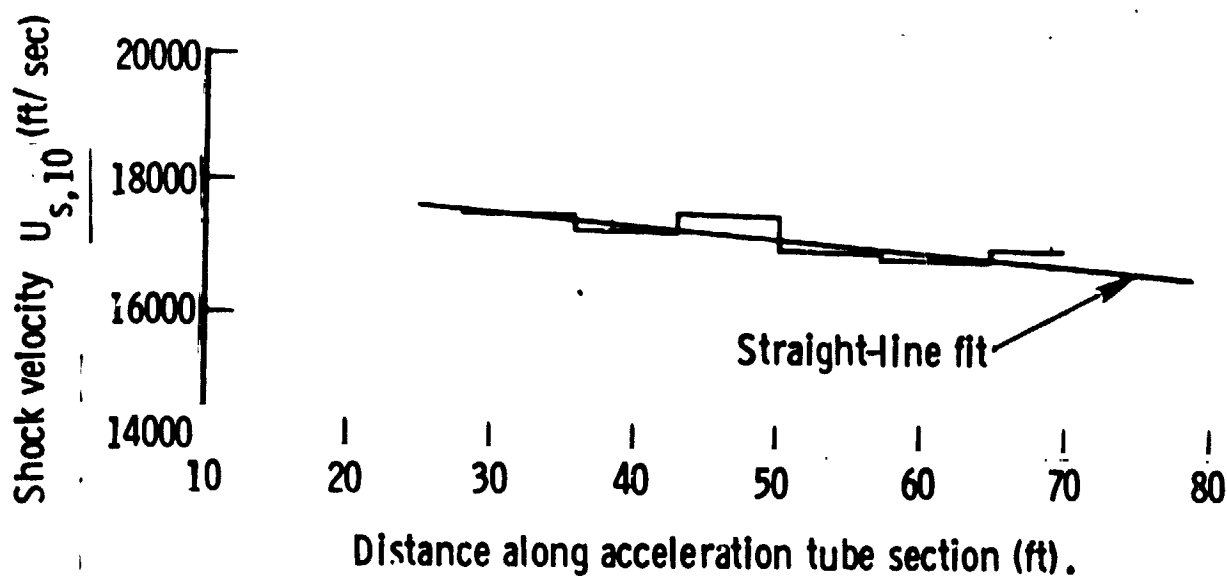
Figure 4.- Variation of shock velocity, $U_{s,10}$, along acceleration section. Test gas: Air, Run 1479.

THIN-FILM HEAT TRANSFER
GAUGES
49.5 m. m.
125.6 m. m.

(TYP.)

QUARTZ SUBSTRATE

88.9 m. m. DIA.

ENTRAN GAUGE

NOSE RADIUS = 6.35 m. m.

40°

THIN-FILM HEAT TRANSFER
GAUGES
59.6 m. m.
125.6 m. m.

(TYP.)

QUARTZ SUBSTRATE

76.2 m. m. DIA.

ENTRAN GAUGE

NOSE RADIUS = 6.35 m. m.

30°
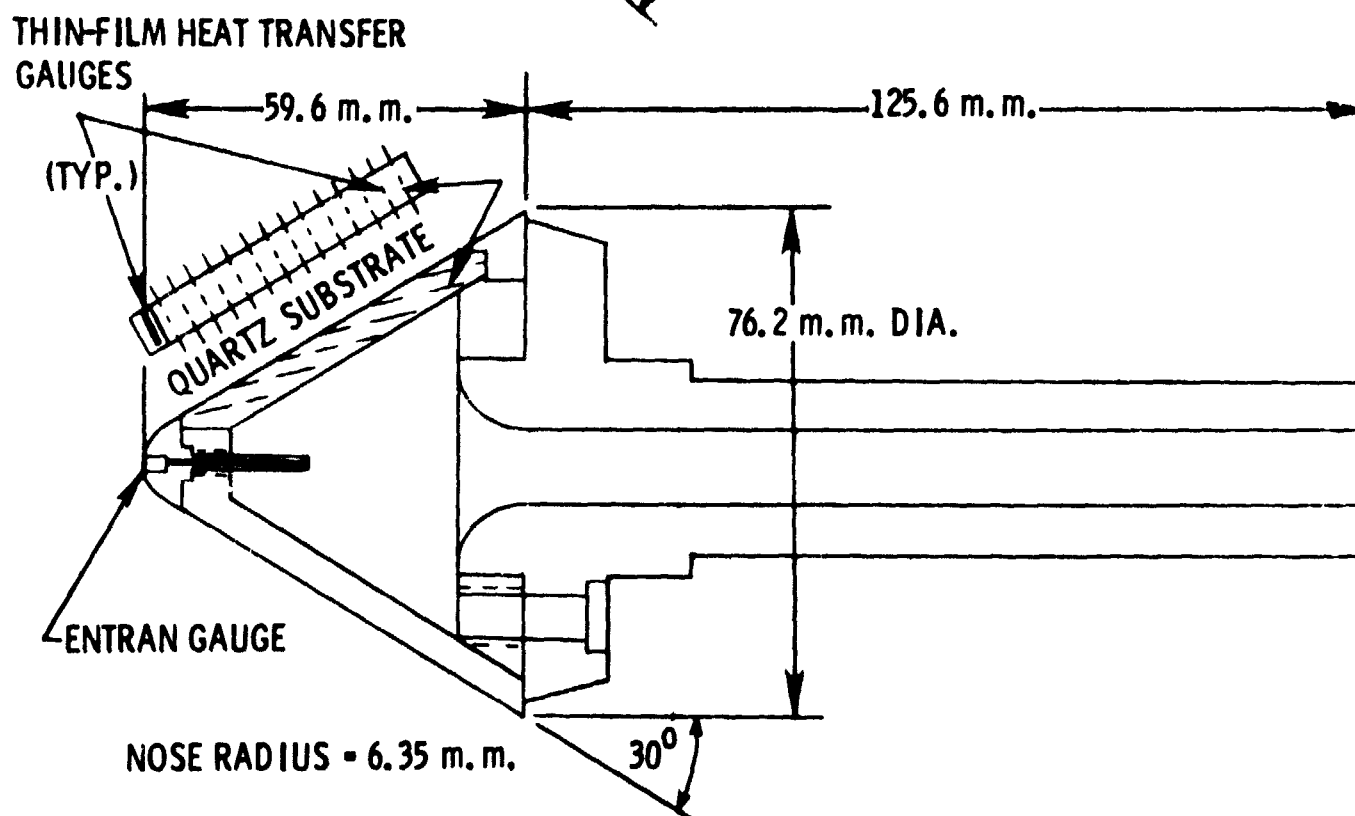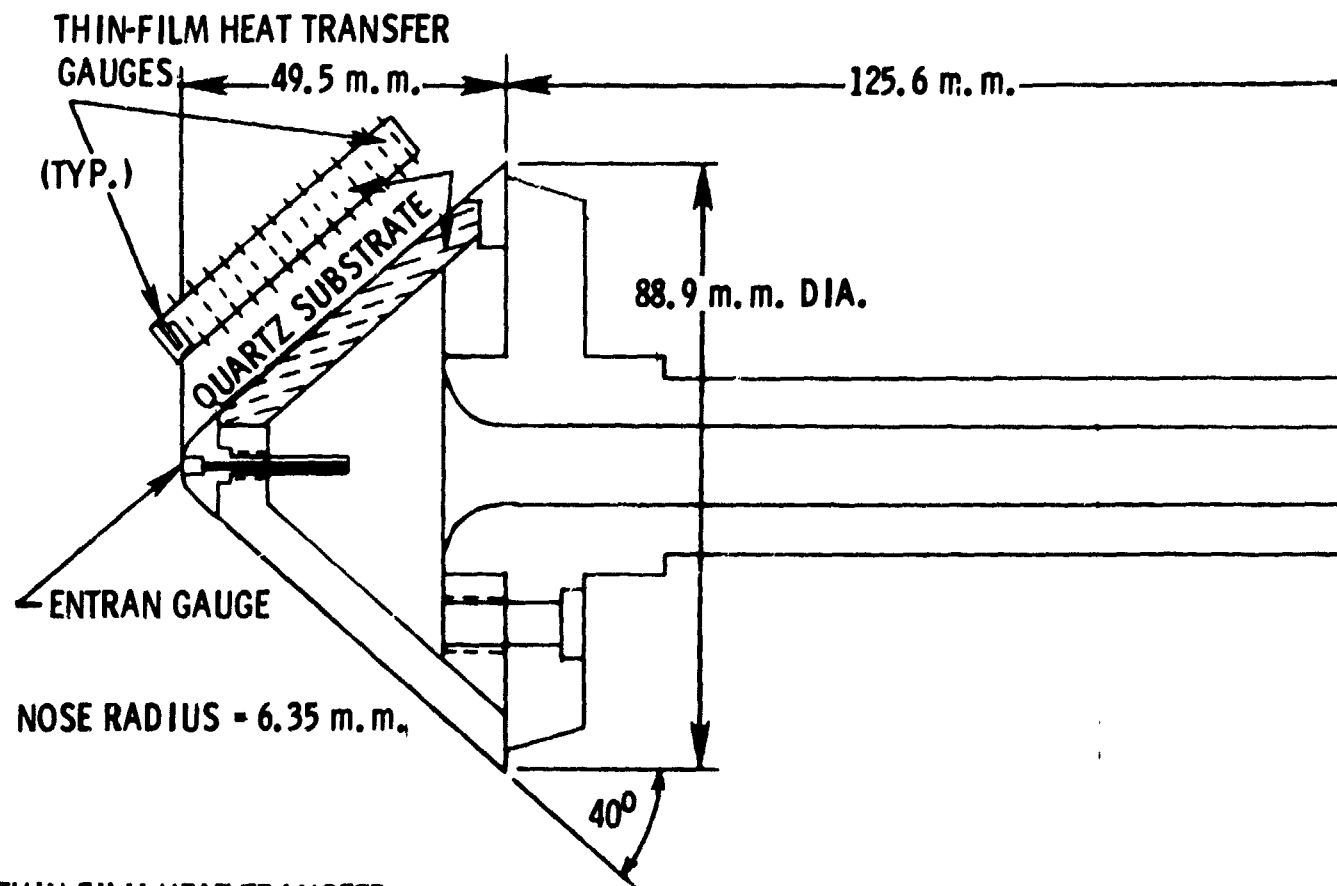
Figure 5.- Details of blunt cone model.

CENTIMETERS
INCHES
0 1 2 3 4 5
0 1 2
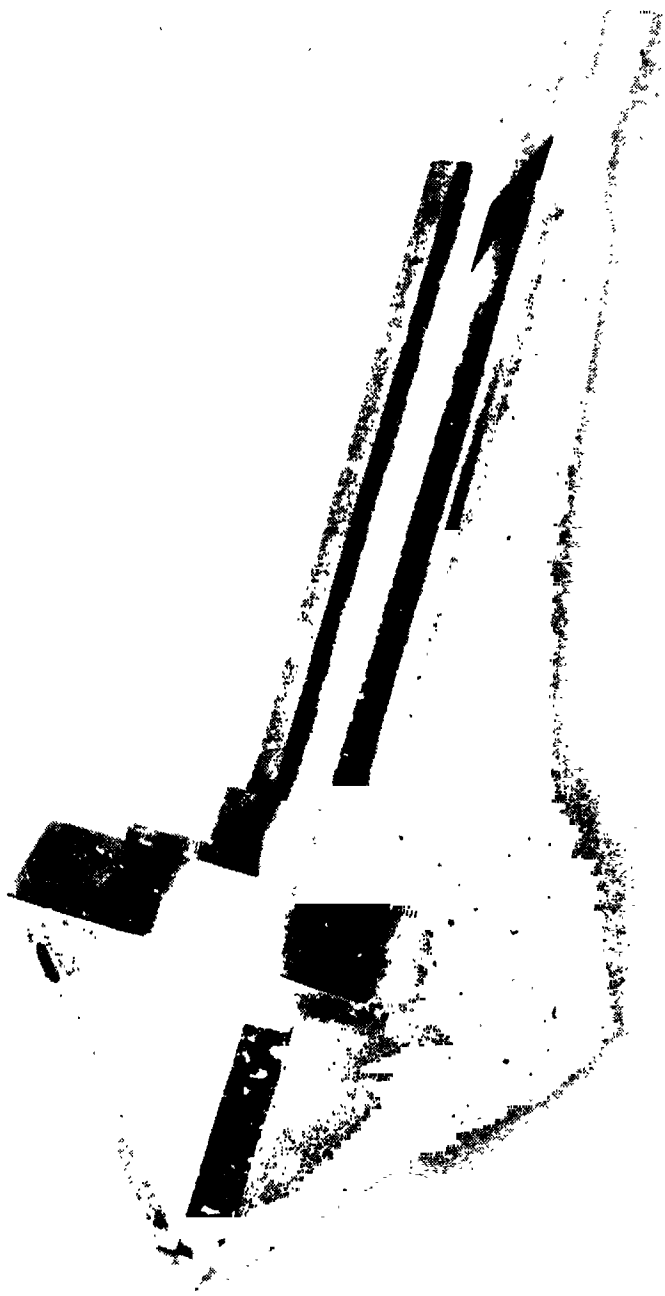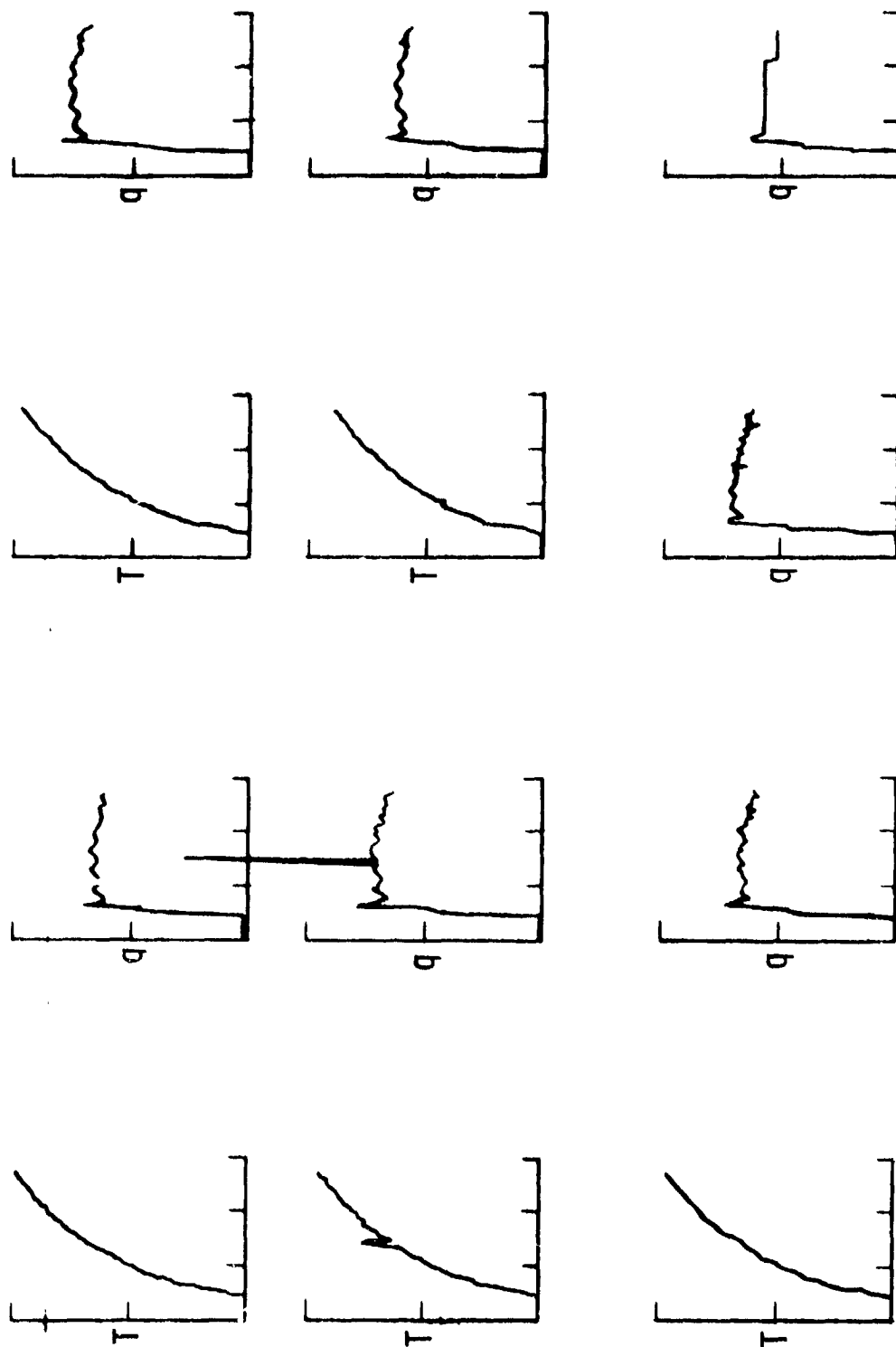
Figure 8.— Sample surface-temperature histories and analog outputs, Run 1494; horizontal scale = 200 microseconds/division; vertical scale = 500 millivolts/division for temperature, 5×10^6 W/m2/division for analog heating rate.
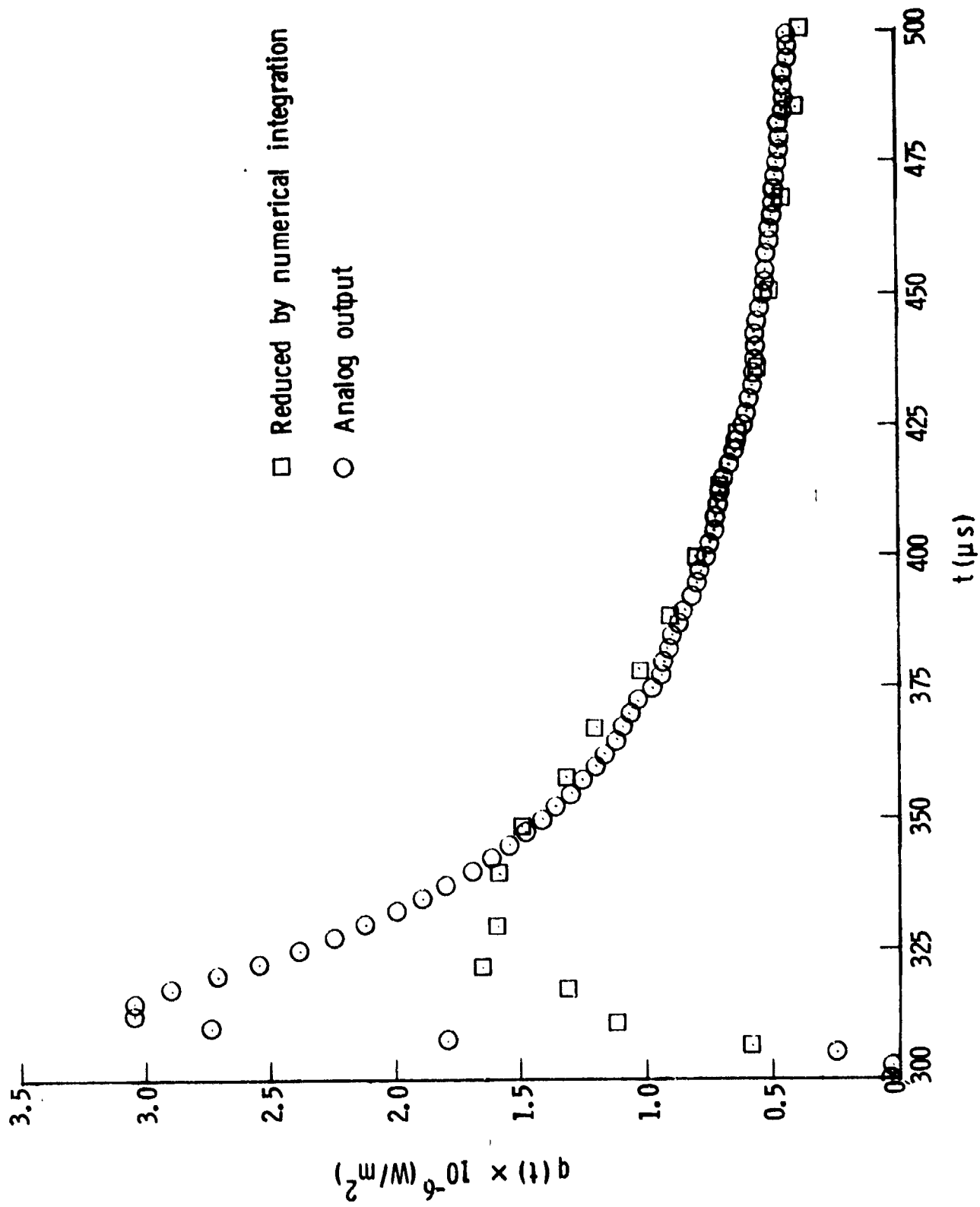
Figure 9.- Comparison of heating rates obtained by numerical integration of shock-tube wall-surface temperature with results of analog circuit.
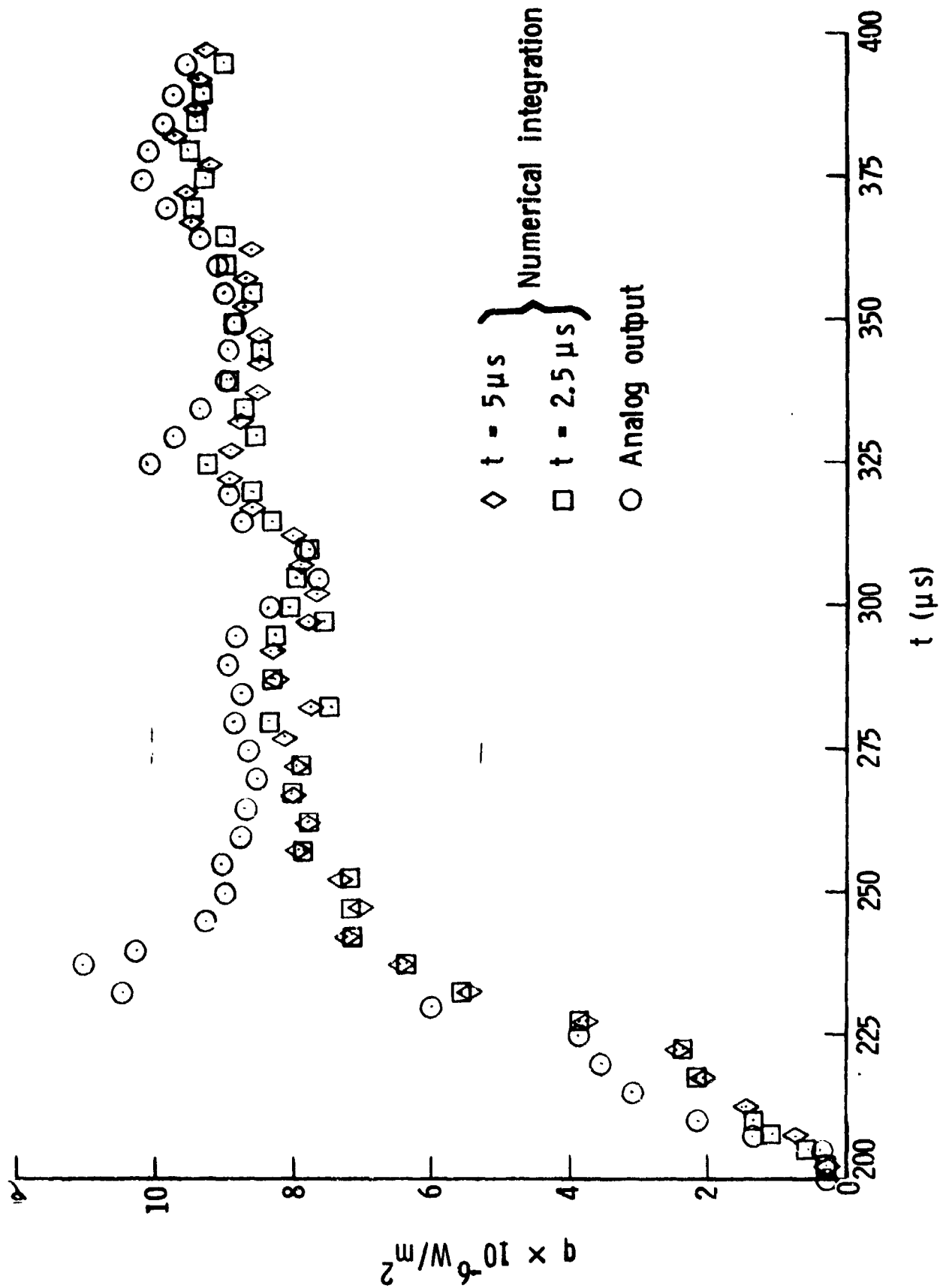
Figure 10.- Comparison of heating rates obtained by numerical integration of stagnation-point temperature history with results of analog output.

Δt = Time interval for signal averaging
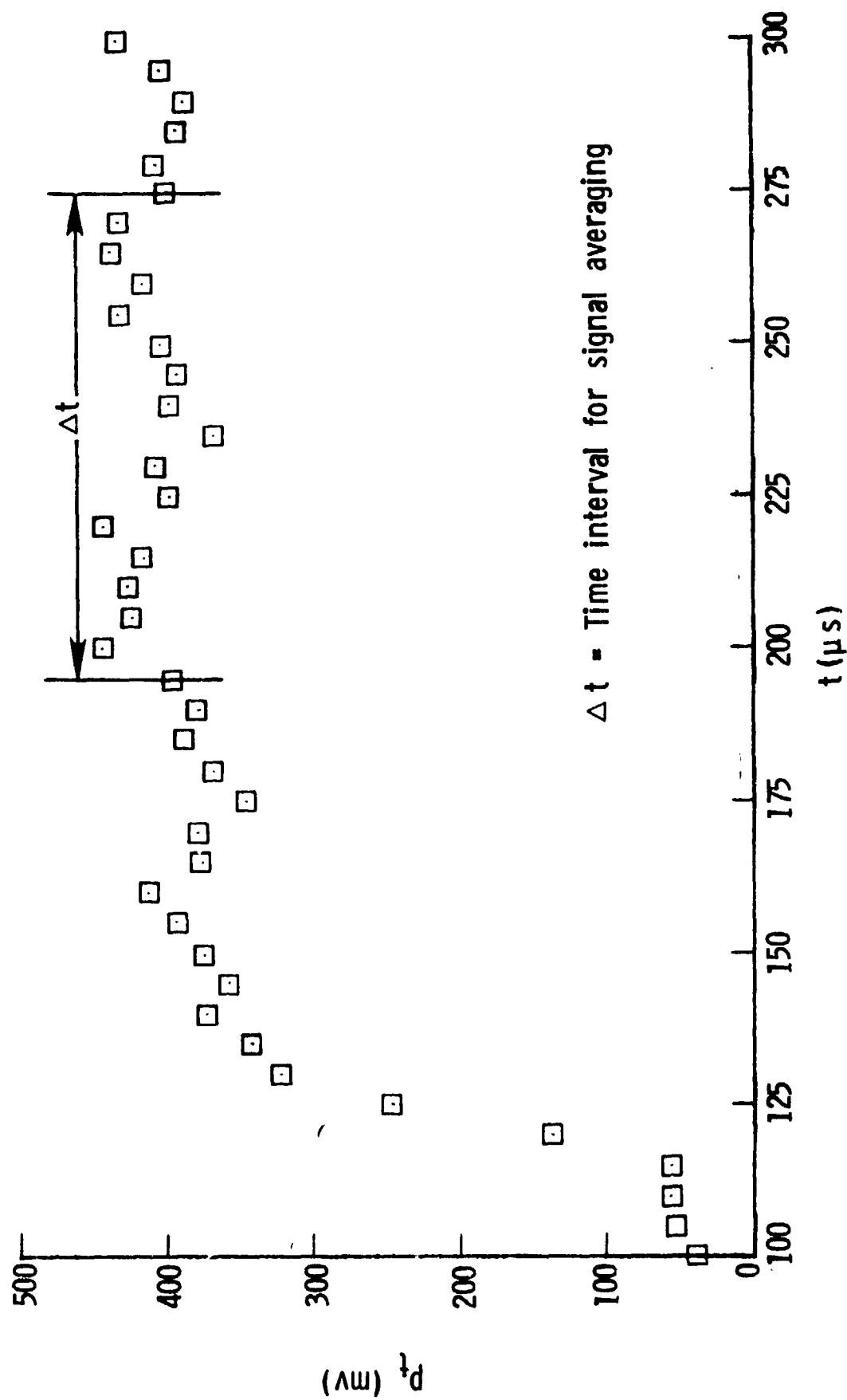
(a) Pitot pressure.

Figure 11.- Illustration of the test period, Δt, as determined from measured flow conditions and heat-transfer rates.
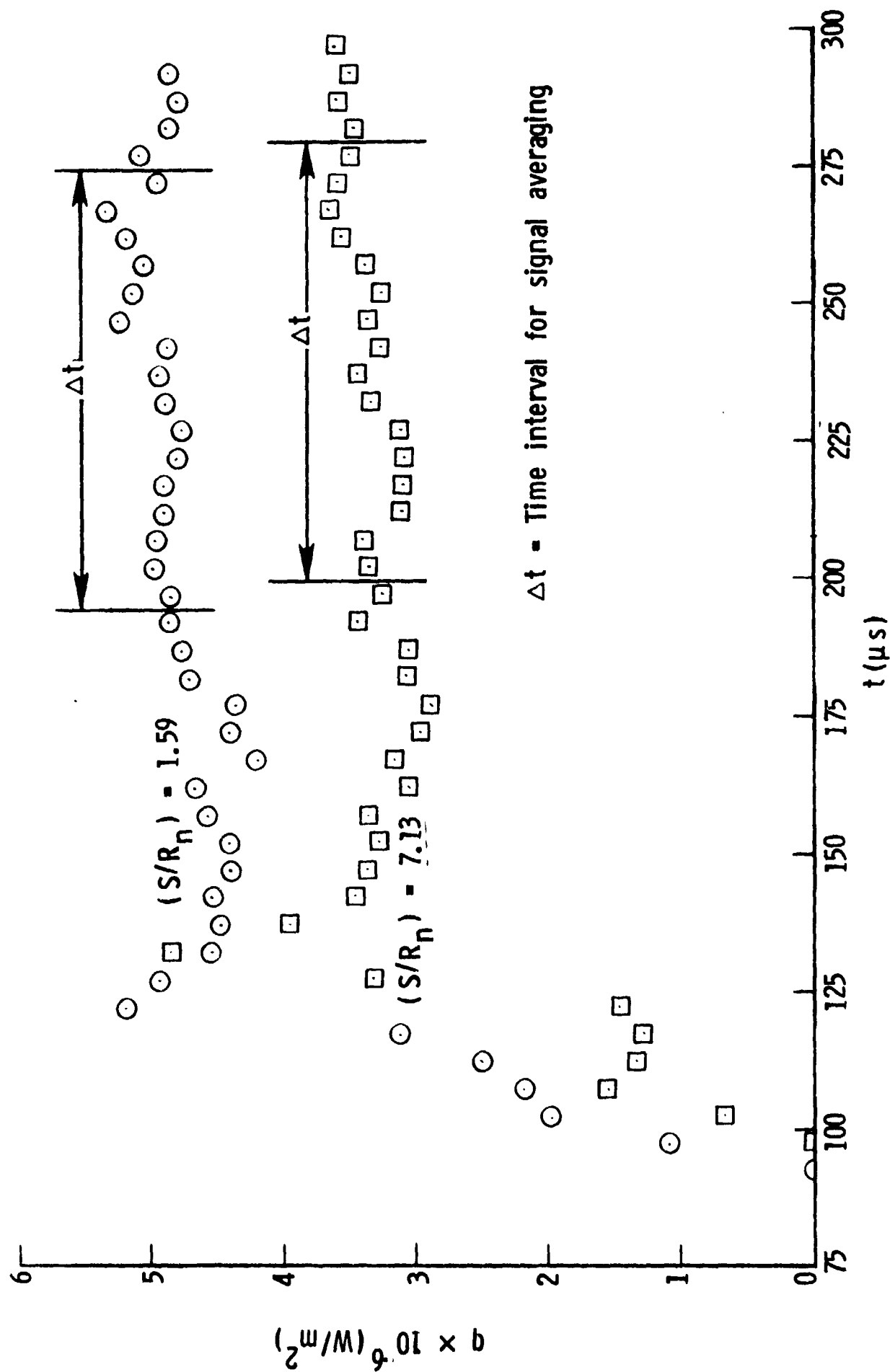
(b) Sample heat-transfer rates.

Figure 11.- Continued.
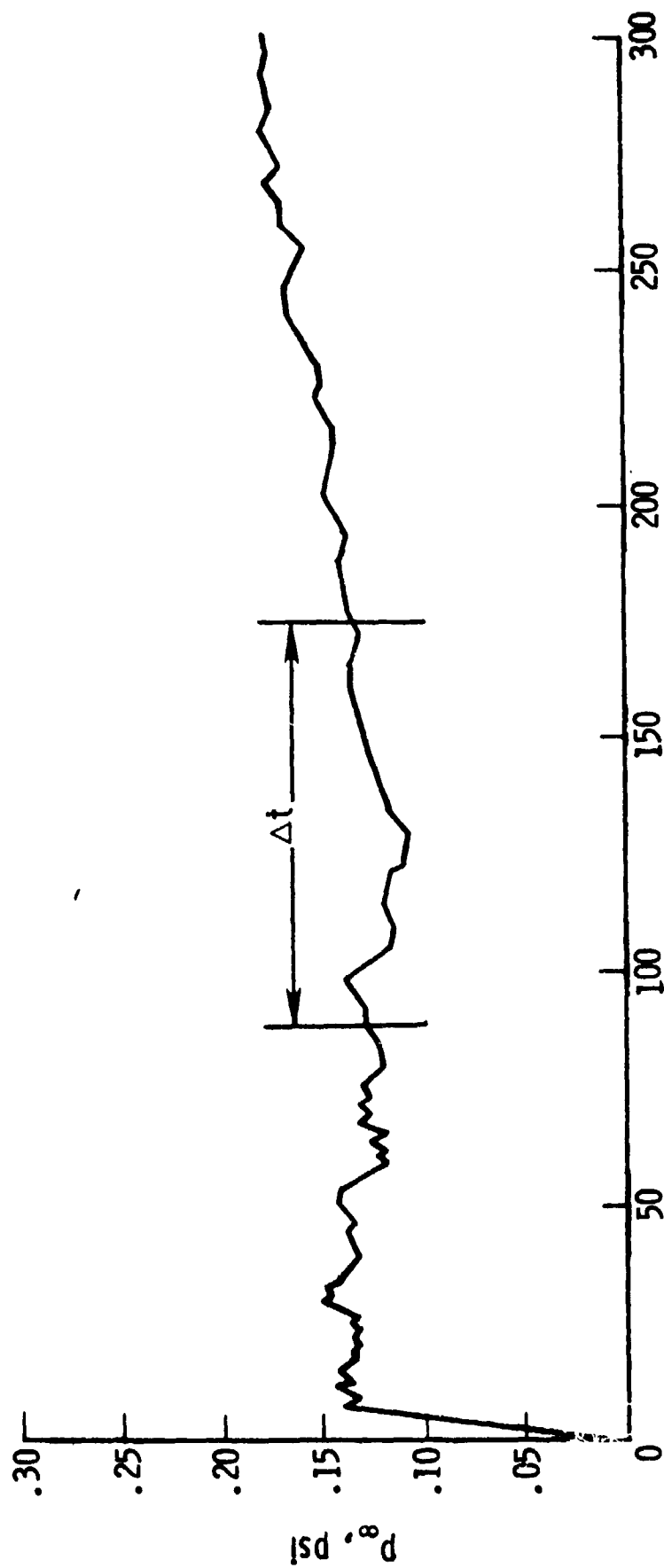
(c) Wall static pressure, P_∞.

Figure 11.- Concluded.
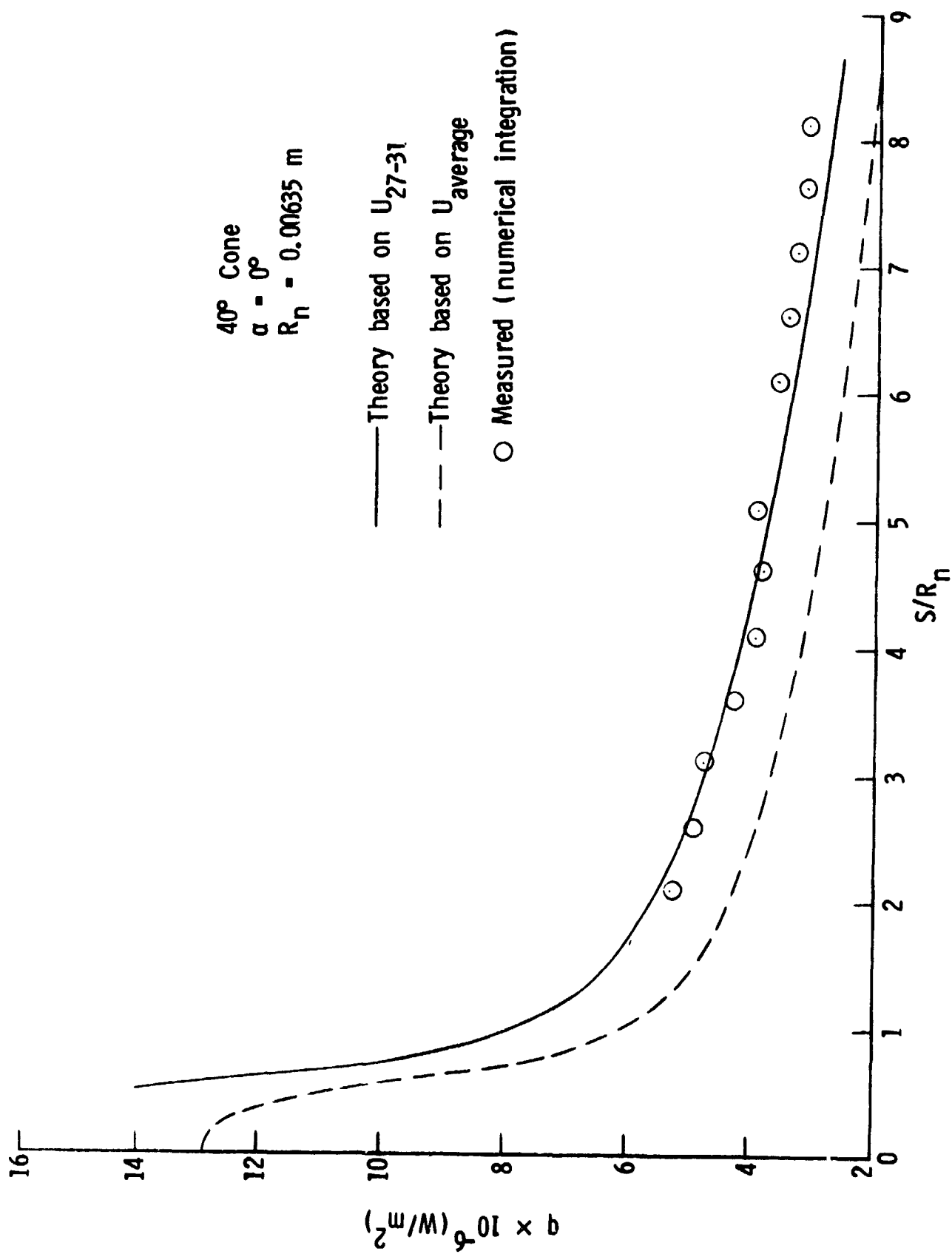
Figure 12.- Comparison of measured heating rates with theory for helium test gas, Run 1475.
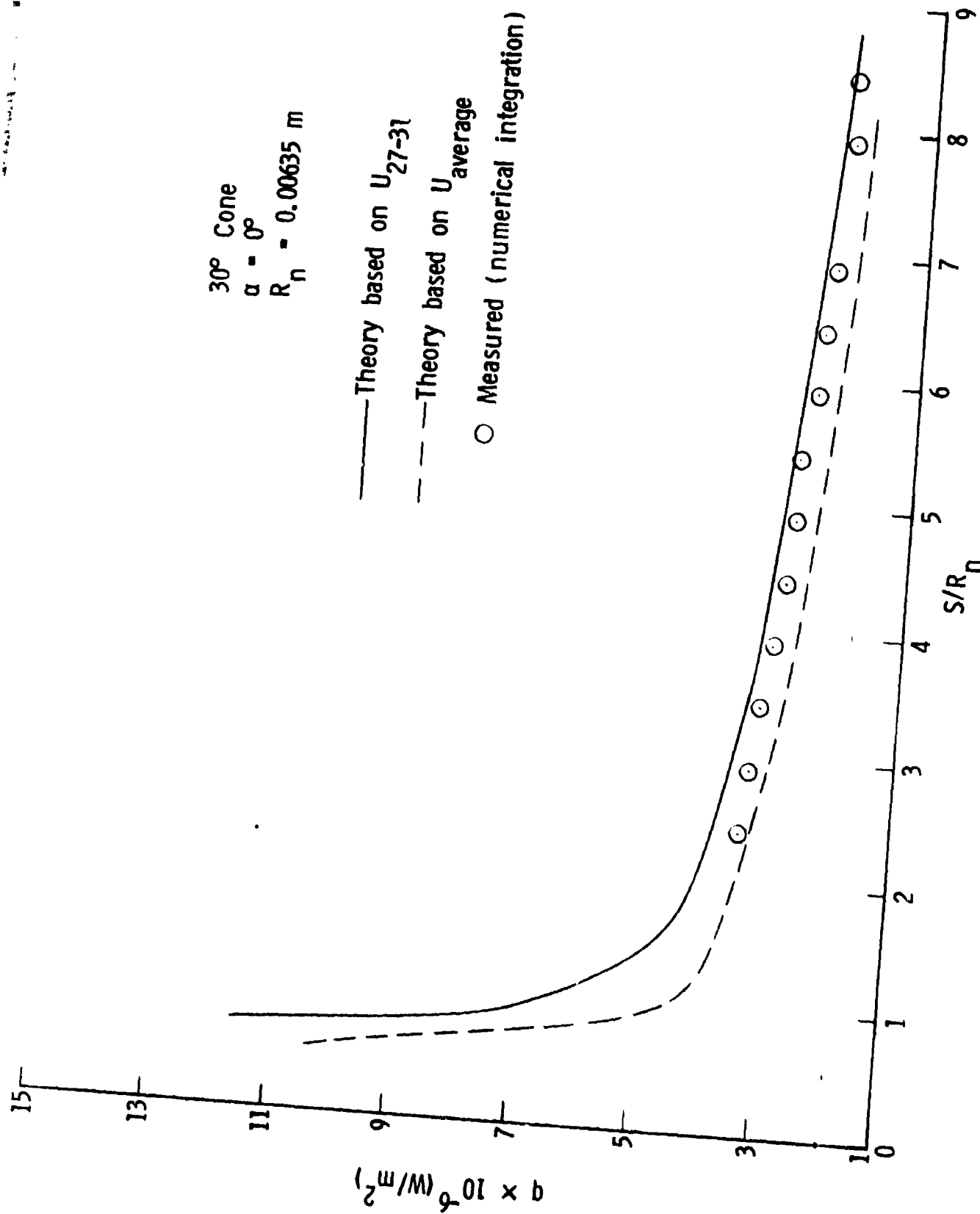
Figure 13.— Comparison of measured heating rates with theory for helium test gas, Run 1476.

$30°$ Cone
$α = 0°$
$R_n = 0.00635$ m

—— Theory based on U_{27-31}

- - - Theory based on $U_{average}$

○ Measured (numerical integration)

S/R_n

$q \times 10^{-6} (W/m^2)$

30° Cone
$\alpha = 0^\circ$
$R_n = 0.00635$ m

—— Theory based on $1.1 \times U_{27-31}$

—·— Theory based on U_{27-31}

— — Theory based on $U_{average}$

$\bigcirc$ Measured (analog network)

$q \times 10^{-6} (W/m^2)$

S/R_n
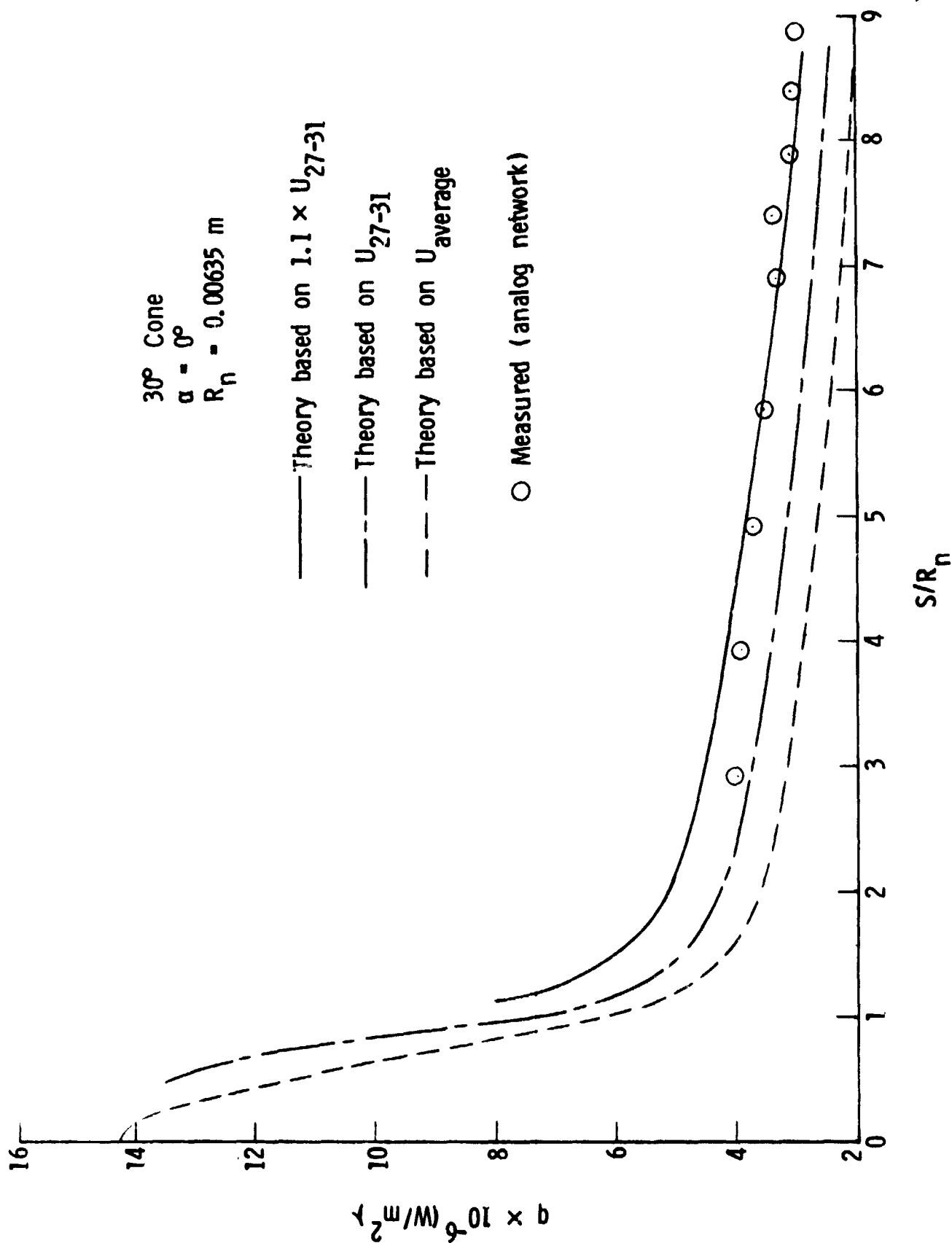
Figure 14.- Comparison of measured heating rates with theory for helium test gas, Run 1491.
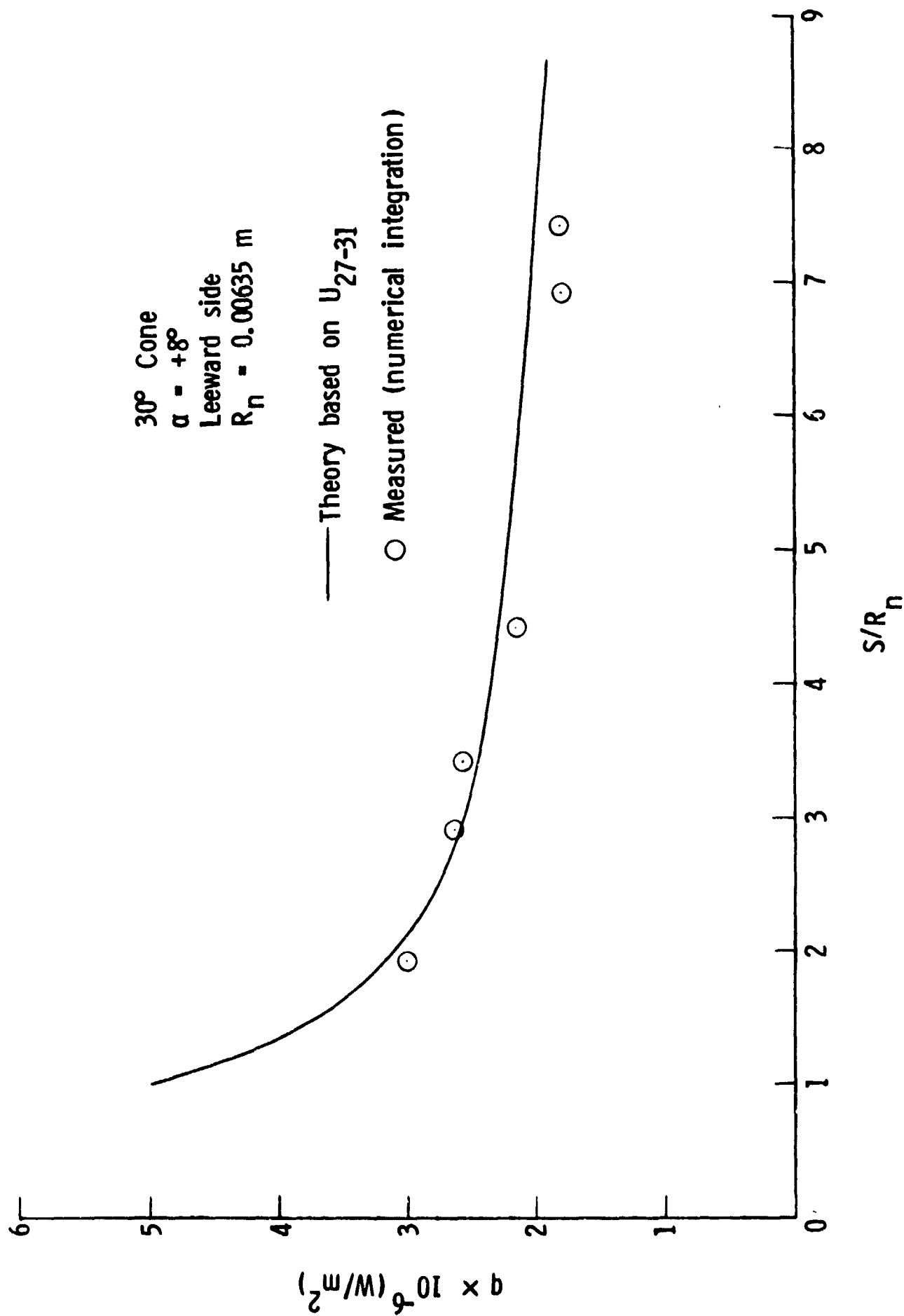
Figure 15.- Comparison of measured heating rates with theory for helium test gas, angle of attack of +8°, Run 1473.
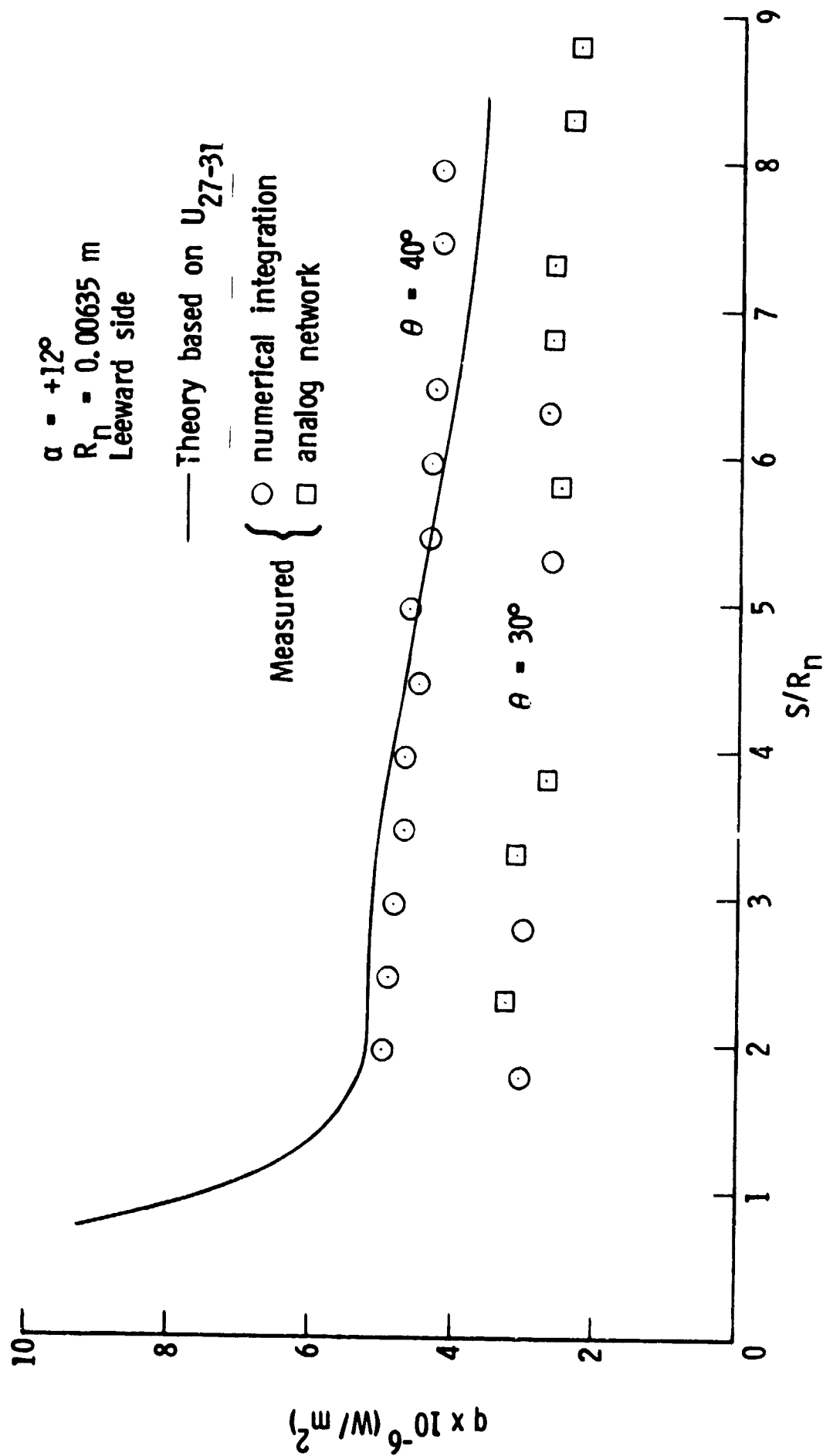
Figure 26.- Comparison of measured heating rates with theory for 30° and 40° cone models at +12° angle of attack. Air test gas, Runs 1477 and 1478.
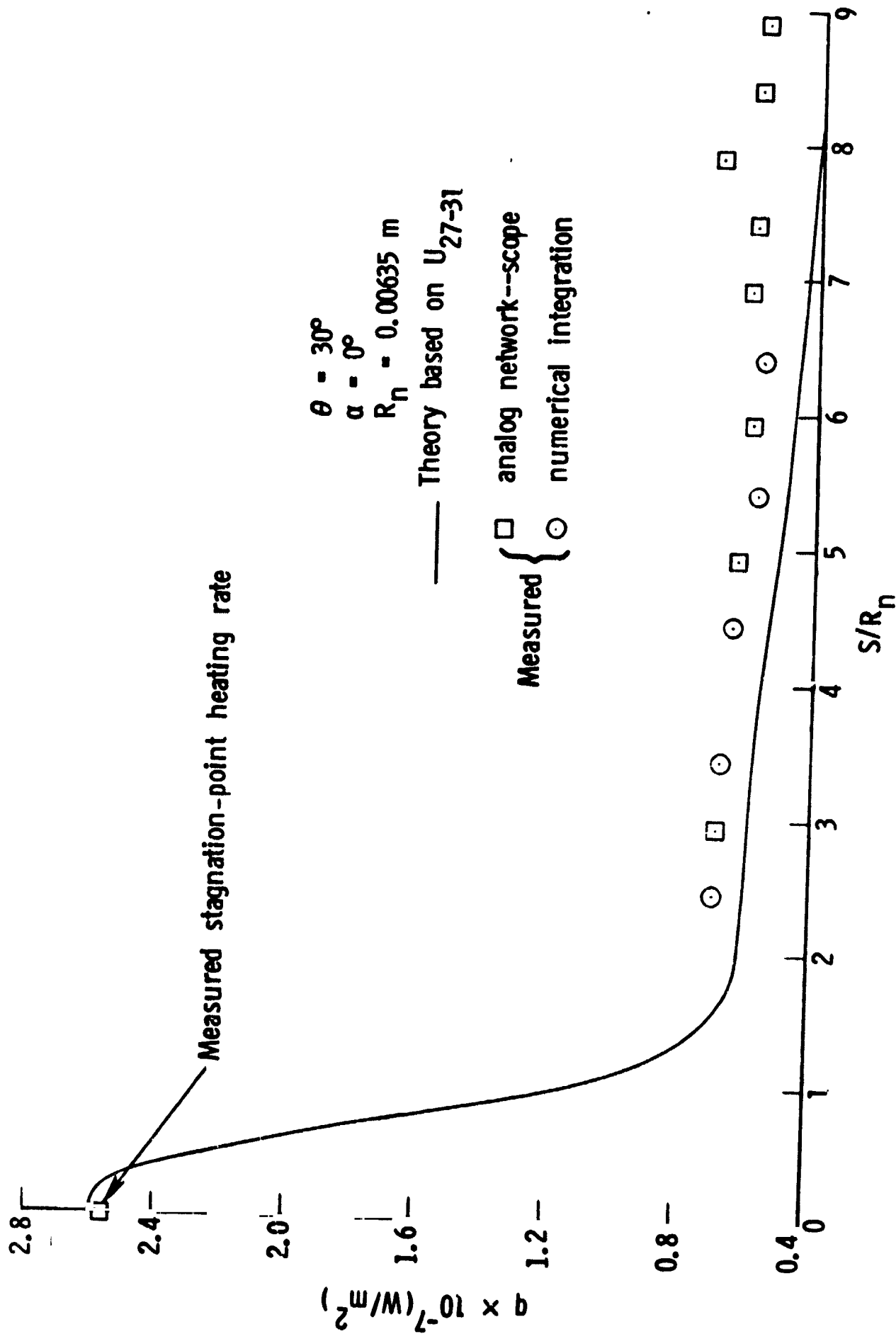
Figure 17.— Comparison of measured heating rates with theory for 30° cone model at 0° angle of attack. Air test gas, Run 1494.
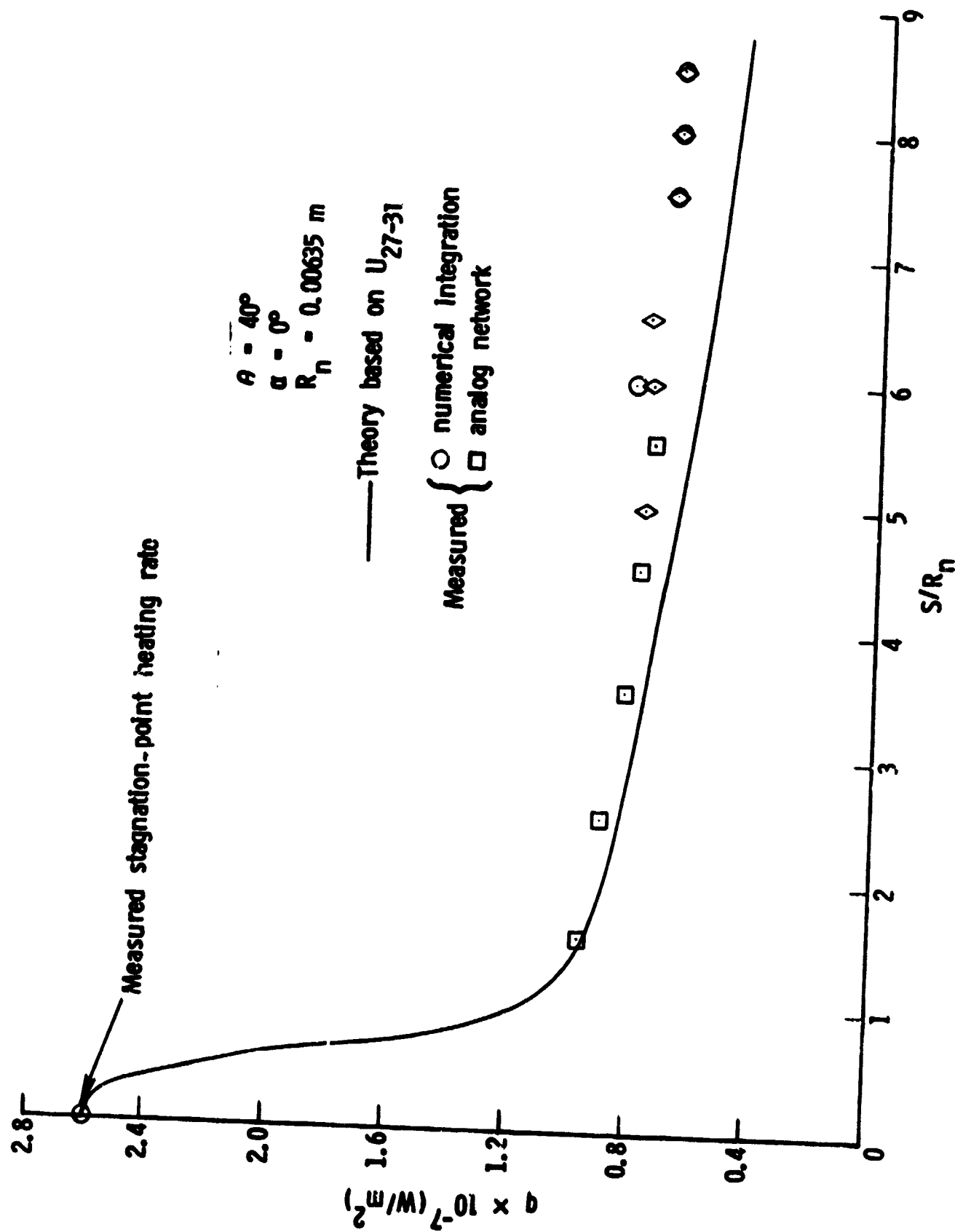
Figure 18.— Comparison of measured heating rates with theory for 30° cone model at 0° angle of attack. Air test gas, Run 1479.
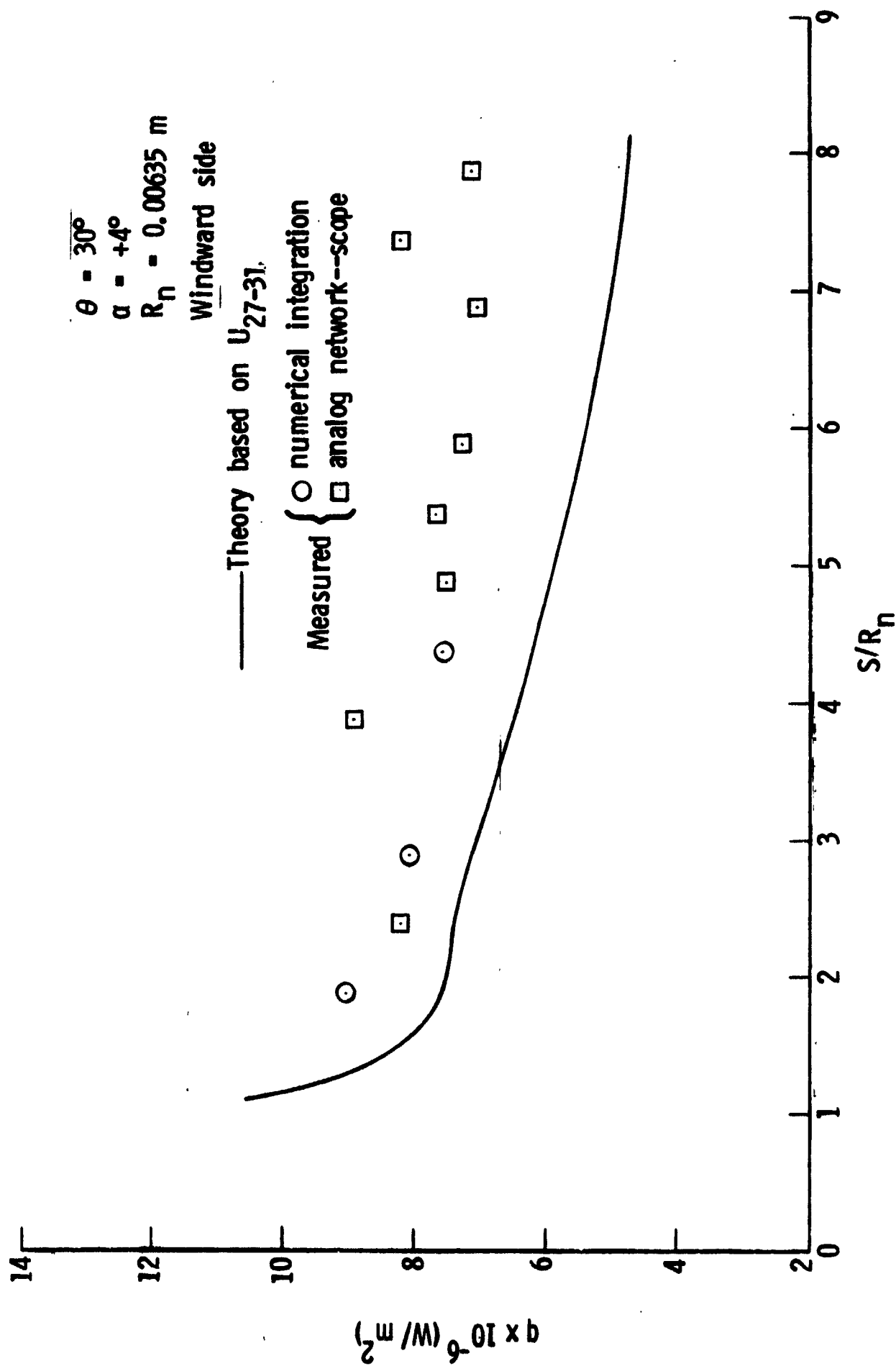
Figure 19.- Comparison of measured heating rates with theory for 40° cone model at 4° angle of attack. Air test gas, Run 1496.
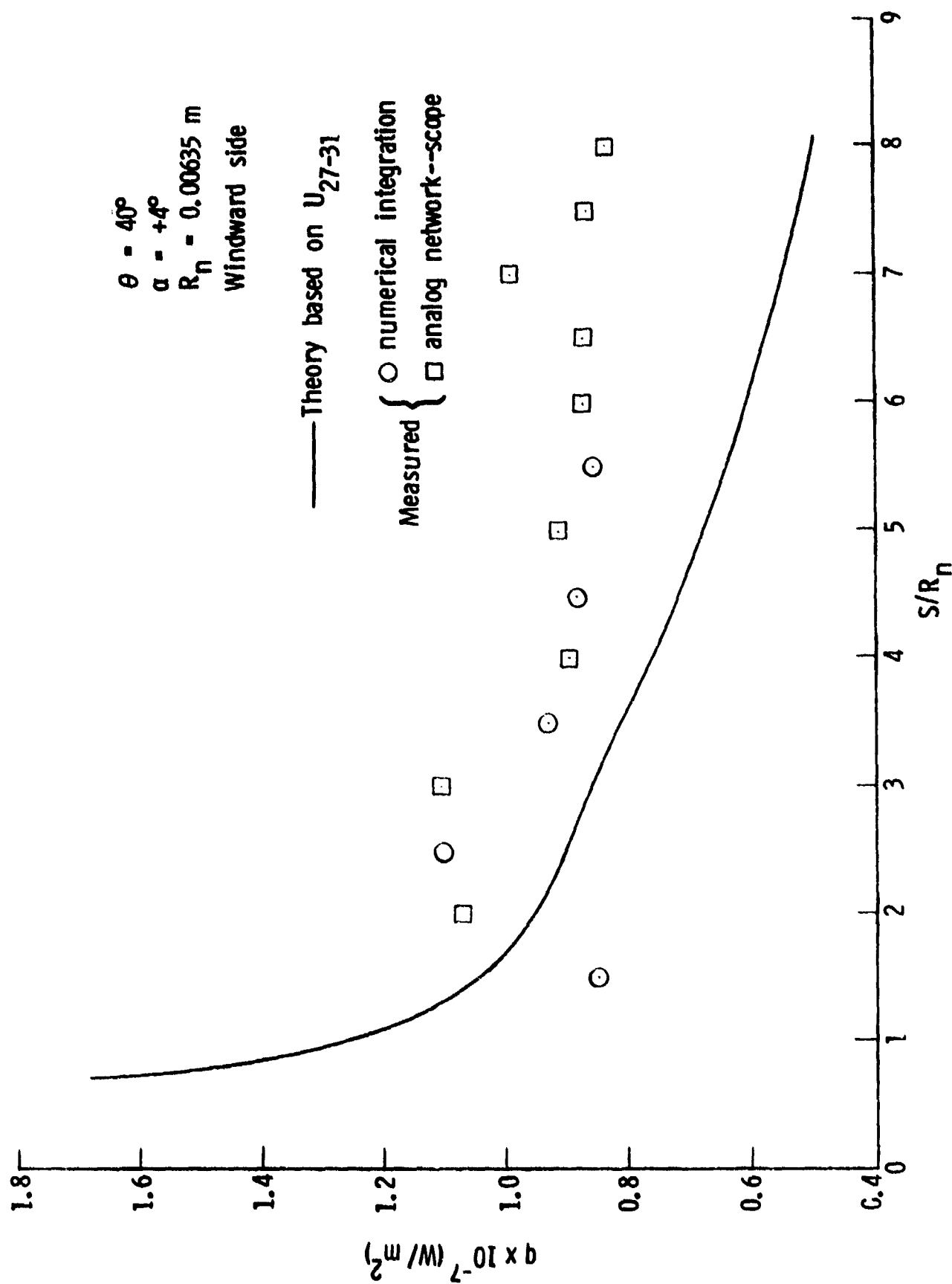
Figure 20.- Comparison of measured heating rates with theory for 30° cone model at 4° angle of attack. Air test gas. Run 1495.